N-terminal region of PetD is essential for cytochrome *b₆f* function and controls STT7 kinase activity via STT7-dependent feedback loop phosphorylation

Afifa Zaeem[1], Yuval Milrad[1], Simon Bütfering[1], Carolyne Stoffel[2], Adrien Burlacot[2,3], Martin Scholz[1], Felix Buchert[1*], Michael Hippler[1,4*]

[1]Institute of Plant Biology and Biotechnology, University of Münster, 48143 Münster, Germany
[2]Biosphere Sciences and Engineering Division, Carnegie Science, Stanford, CA 94305
[3]Department of Biology, Stanford University, Stanford, CA 94305
[4]Institute of Plant Science and Resources, Okayama University, Kurashiki, Japan

[*]Correspondence to: felix.buchert@uni-muenster.de; mhippler@uni-muenster.de

Abstract

The cytochrome *b₆f* complex (*b₆f*) links photosystem I (PSI) and photosystem II (PSII) in the photosynthetic electron transfer chain and is distributed across appressed and non-appressed thylakoid membranes. The *b₆f* also activates the state-transition 7 kinase (STT7), which phosphorylates light-harvesting complex proteins, triggering their migration to enable energy redistribution between PSII and PSI. STT7-dependent phosphorylation has also been observed at T4 in the N-terminal domain of the *b₆f* subunit-IV (PetD), though its functional significance has remained unclear. To investigate its role, we generated several chloroplast mutants. The phosphomimic mutation PetD T4E inhibited STT7 kinase activity, as indicated by the absence of STT7-dependent phosphorylation and the strain being locked in State 1. This reveals a novel feedback mechanism regulating phosphorylation facilitated by STT7. The deletion of five N-terminal amino acids resulted in a comparable inhibition of STT7 activity and, additionally, in the disruption of electron transfer which underscores a crucial role of the PetD N-terminus in *b₆f* function.

Main

Photosynthesis captures light through photosystem (PS) I and PSII along with light-harvesting complexes (LHCI and LHCII). Light energy drives water splitting at PSII and ultimately reduces ferredoxin (FDX) through PSI. In linear electron transfer (LEF), reduced FDX transfers electrons to FDX-NADP(H) oxidoreductase (FNR), producing NADPH for CO_2 fixation and biomass production. In addition, electron transport deposits H^+ in the lumen and separates charges across the thylakoid membrane, thereby generating both a proton gradient (ΔpH) and membrane potential (ΔΨ), which collectively drive ATP synthesis. Electron flow between the photosystems is mediated by the cytochrome b_6f complex (b_6f; reviewed in [1]), which shuttles electrons from plastoquinol (PQH_2) in the plastoquinone (PQ) pool to plastocyanin. Besides small peripheral subunits, the b_6f core comprises cytochrome-*f* (PetA), cytochrome-b_6 (PetB), Rieske iron-sulfur protein (ISP, PetC), and subunit-IV (PetD). High-potential redox centers contrast with low-potential cofactors, including heme c_i at the Qi-site. The latter is the stromal PQH_2 binding pocket opposing the lumenal Qo-site. By cycling protons between sites Qo and Qi, the ΔpH associated with b_6f activity substantially contributes to ATP production for CO_2 fixation. Moreover, the c_i heme within the Qi-site is relevant for cyclic electron flow (CEF) and the b_6f complex may function as a FDX-PQ reductase (FQR) in CEF [2,3].

The lumen acidification stemming from photosynthetic electron flows is important for efficient photoprotection under conditions of excess excitation energy: it establishes "photosynthetic control" at the Qo-site where PQH_2 oxidation (and therefore electron flow) ceases at acidic pH [4,5], and it reduces photochemistry by stimulating controlled heat dissipation via non-photochemical quenching (NPQ) [6-8]. Moreover, the b_6f is linked to state transitions (ST) – another photoprotective mechanism to cope with overexcitation [9]. During this process, LHCII migrates between PSII and PSI upon its phosphorylation by the thylakoid-bound STT7 kinase [10,11]. STT7 is activated by a reduced PQ pool while specific phosphatases act as STT7 antagonists [12]. The activity of the STT7 kinase is regulated by its transmembrane domain, with a disulfide bond between two lumenal cysteine residues being essential for its function [13]. Active discussions and research on the kinase redox regulation are ongoing [14-16]. Recently it was shown that ST involve PetD residues N122, Y124, and R125 in the stromal "fg Loop", linking helices F and G of this b_6f subunit [17]. Moreover, the C-terminus of the b_6f subunit PetB interacts with the fg Loop in PetD, thereby facilitating STT7 activation [18]. Mechanistically, binding of STT7 to b_6f enhances its autophosphorylation and R125 is directly involved in this process. In this report we focus on another stromal element of b_6f in the model green microalgae *Chlamydomonas reinhardtii* (see Extended data Fig. 1): The N-terminus in PetD where T4 undergoes phosphorylation in an STT7-dependent manner [19] (see also Extended data Fig. 2).

To investigate the functional significance of STT7-dependent phosphorylation at PetD T4, we created PetD site-directed mutants T4A and T4E to mimic constitutive absence and presence of phosphorylation, respectively. Moreover, the function of the five N-terminal residues was addressed in a truncation mutant (ΔN) whereas the wild-type PetD (WT) was used as control. To achieve this, chloroplast transformation targeted recombination within the *petD* locus, incorporating an *aadA* cassette to confer spectinomycin resistance for selection. The recipient strain used carried a six-histidine tag at the C-terminus of PetA [20] for optional b_6f purification. Spot test on TP plates, requiring photoautotrophic growth, revealed that mutant strains T4A and T4E performed similar to WT under normal (40 µmol photons m^{-2} s^{-1}) and moderate high light (200 µmol photons m^{-2} s^{-1}; Extended data Fig. 3a). In contrast, the ΔN strain showed a growth deficit at both light intensities compared to the other strains. Proteomic analysis showed no significant differences in the levels of PetD and other core b_6f subunits between WT, T4A, and T4E (Extended data Fig. 3b). Compared to WT, only PETO was significantly downregulated in ΔN, while LHCSR1 was markedly upregulated in T4E relative to T4A (Extended data Fig. 4). Given the observed growth phenotypes and the changes in the amounts of the CEF effector protein PETO [21] and LHCSR1 – required for pH-dependent NPQ [22] – key photoprotection pathways associated with b_6f function might be altered in the mutants. To this end, we first present data investigating ST as they require the physical presence of b_6f [23], and then performed electron transfer measurements to directly assess b_6f activity in the mutants.

To assess if ST are affected in the mutants, the antenna redistribution between PSI and PSII was measured using 77 K fluorescence emission spectroscopy [24] after cells were shifted to either State 1 or State 2 inducing conditions (Fig. 1). Thereby, an increase in antennae size under State 2 versus State 1 conditions was observed for WT and T4A (Figs. 1a, 1b). In contrast, T4E and ΔN strains displayed no differences in their 77 K fluorescence emission spectra, indicating they were unable to perform ST (Figs. 1c, 1d).

The 77 K data suggest impaired STT7-dependent phosphorylation in T4E and ΔN strains, which was supported by an additional phospho-proteomic analysis of PetD variants. Here, absence of STT7 phosphorylation levels of S569 and T571 (Extended data Fig. 5) coincided with lack of ST. To look for STT7 targets in our phospho-proteomic search we also included a CRISPR/Cas9 *stt7* KO mutant and its respective WT in the analysis as a control (Extended data Fig. 6). Differential expression analysis revealed STT7-dependent phosphorylation sites with significant upregulation or downregulation in samples from State 2 conditions (absolute log2-fold change ≥ 1, $p < 0.05$, Extended data Tab. 1, Extended data Fig. 2). The chloroplast protein PTAC16 showed the highest number of differentially regulated phosphorylation sites. Generally, decreased or absent phosphorylation of PTAC16 was observed in the *stt7* strain (Extended data Fig. 2). T4E and ΔN showed similar PTAC16 patterns but retained some phosphorylation at WT sites (Fig. 2). The

101 T4A strain showed no significant differences. Phosphorylation differences varied between strains
102 and may depend on genetic background. PTAC16 was recognized as a protein of the plastid
103 transcriptionally active chromosome complex [25], and has also been identified as a substrate of
104 STN7 in Arabidopsis [26]. WT cells showed substantially higher levels of dual T7/T11
105 phosphorylation on LHCB4 compared to *stt7*, with a 6.8-Log2fold change. The *stt7* mutation had
106 widespread effects, eliminating phosphorylation at numerous key sites. These included single
107 phosphorylation sites on proteins like PetD (T4), PETO (T161/S164), and ANR1 (T171), as well
108 as several critical threonine clusters - notably the T33/T35/T37 region of LHCB4, T23/T36 of
109 LHCB5, and the N-terminal phospho-site cluster in LHCSR3 (S26/S28/T32/T33/T39) [27]. LHCB5
110 retained only minimal phosphorylation at T20 in the *stt7* background (Extended data Fig. 2). The
111 ΔN and T4E strains also showed distinct phosphorylation patterns. Some sites undetectable in
112 *stt7* were similarly absent in these strains – such as ANR1 (T171) in ΔN, and LHCBM1 (T27) in
113 both ΔN and T4E. PETO showed an interesting pattern where T185 phosphorylation occurred
114 only in conjunction with S187 phosphorylation in *stt7* and ΔN, though at lower levels than in
115 wild type. The ΔN and T4E strains both exhibited reduced phosphorylation across several
116 thylakoid proteins, including LHCBM5 (double phosphorylation of S28+T33), PSB34 (T39),
117 PSAG (T71), and PSBR (T37, S43, and T37+S43), while also showing decreased STT7
118 autophosphorylation at S569 and T571 (Extended data Fig. 5). ΔN specifically showed decreased
119 phosphorylation of LHCBM3 and LHCBM6 but was the only strain with augmented
120 phosphorylation at T72 of PSAG. The T4A strain behaved distinctly, with most of the
121 aforementioned phosphorylation sites remaining unchanged, though it uniquely showed
122 substantially increased phosphorylation of PSBR (T39, S43, and T37+S43) compared to the other
123 strains. Most of the STT7-dependent phosphorylation sites listed above had also been previously
124 identified [19,28].

125 While most phosphorylations of thylakoid proteins decreased in the ST-deficient mutants, PSBD
126 (T2) showed increased phosphorylation in *stt7* (5.5-Log2fold change), confirming previous
127 results obtained from a different *stt7* mutant (Extended data Fig. 2, and [19]). PSBD
128 phosphorylation also increased in T4E (3.4-fold log2), while ΔN and T4A strains showed no
129 significant differences. Previous studies have also documented STT7-dependent phosphorylation
130 sites on threonine residues in LHCBM1, LHCBM4, 6, 8, 9, LHCBM3, and LHCBM5 [19,28]. The
131 STT7-dependent phosphorylation of LHCBM1 and LHCBM5 have been structurally resolved in
132 the PSI-LHCI-LHCII ST complex [29]. Thus, we conclude that a single amino acid substitution
133 mimicking constitutive phosphorylation in PetD (T4 to E4) markedly altered phosphorylation
134 patterns of STT7-dependent substrates.

135 To assess functional consequences of the alterations in the engineered strains, we measured
136 photosynthetic electron transfer rates (ETR) using electrochromic shift (ECS) signals. In

137 photoautotrophic cells, neither T4A nor T4E were different from WT which suggests that T4
138 does not impact ETR directly (Figs. 3a, 3b). However, ETR in ΔN slowed significantly 30–50 ms
139 after light exposure in cells grown under oxic conditions (Fig. 3a). Under anoxic conditions,
140 which favour CEF, ETR increased initially but reached a lower steady state, with the initial boost
141 notably reduced in ΔN (Fig. 3b). This suggests that the PetD N-terminus ensures ETR via b_6f.
142 Redox kinetics of P700 were also monitored (Figs. 3c, 3d). In ΔN, P700 oxidized rapidly at light
143 onset, followed by slow re-reduction in the dark, indicating donor-side limitation under both oxic
144 and anoxic conditions. Steady-state ETR (Figs. 3a, 3b) were established in the presence of a
145 substantial P700 acceptor-side limitation, except in ΔN (Figs. 3c, 3d). This donor-side limitation
146 in ΔN persisted even with the H^+/K^+ exchanger nigericin (Extended Data Figs. 7a, 7b), ruling out
147 a pH-dependent photosynthetic control mechanism. Addition of DCMU and nigericin resulted in
148 rapid P700 oxidation across all strains, slightly faster in ΔN (Extended Data Figs. 7c, 7d),
149 suggesting impaired b_6f function in LEF and CEF.
150 To confirm whether these ETR and P700 redox kinetics differences arose from b_6f dysfunction,
151 we assessed b_6f electrogenicity and redox kinetics (Extended Data Fig. 8, Fig. 4). ECS rise from
152 Q-cycle activity was impaired only in ΔN, despite the presence of heme c_i (Extended Data Figs. 8
153 and 9), the terminal electron acceptor in the low-potential chain [30]. Under oxic conditions, WT *b*-
154 hemes showed a transient reduction (~10 ms) before net oxidation (~16 ms half-life), while
155 cytochrome-*f* reduction (~6 ms half-life) began ~1 ms post-flash (Fig. 4a). In ΔN, the apparent *b*-
156 heme reduction was enhanced because their oxidation slowed ~20-fold (Fig. 4b). This coincided
157 with a ~10-fold slowdown in cytochrome-*f* reduction (Fig. 4b), indicating Qi-site impairment
158 affecting the Qo-site as has been shown in b_6f [3,31] and the related cytochrome-bc_1 complex [32,33].
159 Under anoxic conditions, WT displayed flat *b*-heme signals in the first 10 ms, followed by
160 accelerated oxidation (Fig. 4c), consistent with prior findings [3,31]. In ΔN, a redox-inactive low-
161 potential chain caused a ~25-fold slowdown in the high-potential chain, as reflected in
162 cytochrome-*f* reduction (cf. Figs. 4c, 4d).
163 This slowdown of electron transfer within b_6f very likely explains the significantly diminished
164 ETR and enhanced P700 donor side limitation (Fig. 3) as well as the strong impact on
165 electrogenicity of the complex when the N-terminus in PetD is truncated (Extended Data Fig. 8).
166 The reason remains to be determined but recent cryo-EM structures of spinach b_6f at 1.9 Å and
167 2.2 Å resolution have revealed that PQ does not make direct contact with the heme c_i at the Qi-
168 site [34]. Instead, the Qi-site is connected to water channels that link to the aqueous exterior of the
169 enzyme, suggesting that binding of PQ at the Qi-site displaces water through these channels. It
170 has been proposed that, upon entering the Qi-site, PQ pushes water molecules out of the cavity in
171 a piston-like fashion. The only remaining water molecule, coined wat1 [34], is crucial for allowing
172 the quinone ring to adopt an orientation that facilitates both electron and proton transfer. The

173 binding of wat1 is guided by PetD D35 which is believed to donate H^+ to wat1 since it is
174 surrounded by several polar residues.

175 The PetD N-terminus we studied is exposed to the aqueous phase, contains two lysine residues,
176 and is positioned near PetD D35. Our findings suggest that the ΔN truncation could influence the
177 entry and exit function of the water channel and/or affect the functional properties of PetD D35
178 itself. This could, in turn, impair electron injection and ejection from the low-potential chain,
179 potentially slowing down electron transfer through the b_6f as observed in the kinetic data (Fig. 4,
180 Extended data Fig. 8). It may also explain why STT7 kinase is not activated in the ΔN mutant
181 (Fig. 2b) as the turnover of the Qo-site was significantly slowed. In line, it has been previously
182 described that a strong impairment in PQH_2 oxidation at the Qo-site of b_6f prevents activation of
183 STT7 [35].

184 Intriguingly, in the ΔN and T4E strains, STT7 autophosphorylation at S569 and T571 was
185 significantly reduced. The failure to modulate these novel phospho-sites may be mechanistically
186 linked to the loss of STT7 kinase activity. Thus, our data highlight the importance of STT7-
187 dependent phosphorylation, which is negatively affected by the phosphomimic T4E mutation,
188 while the negative charge at PetD position 4 does not influence b_6f function. Notably, the failure
189 of STT7 to operate in ΔN, did not lead to the phosphorylation of PSBD T2, as seen in *stt7*
190 (Extended data Fig. 2 and [19]) and PetD T4E (Fig. 2). In some instances, such as PSBR, the T4A
191 showed increased phosphorylation, implying that PetD T4 phosphorylation may function as a
192 feedback regulator during STT7 activation. The dependence of STT7 function on PetD T4
193 phosphorylation reveals a novel feedback regulation mechanism, complementing previously
194 described STT7 autophosphorylation pathways involving other b_6f structural elements in stromal
195 proximity [17,18].

196 In conclusion, we found that the N-terminal region of PetD is essential for cytochrome b_6f
197 function. We further conclude that STT7-dependent phosphorylation of PetD T4 regulates STT7
198 kinase activity, establishing a feedback loop that adds a new layer to the intricate regulation of b_6f
199 and STT7 kinase. This feedback loop transiently reduces STT7-dependent phosphorylation via
200 the phosphorylation at PetD T4, which coincides with increasing PSBD T2 PSII core
201 phosphorylation, as previously described for vascular plants [36] and algae [37]. As a result, PetD T4
202 phosphorylation mediates a balance between STT7-dependent ST and other processes, as
203 indicated by PSBD T2 PSII core phosphorylation.

204

205 **Methods**

206

207 **WT Plasmid construction**

208 The *petD/trnR1* region (481 bp upstream and 1032 bp downstream of *petD*) was amplified from
209 WT chloroplast DNA using restriction site-containing primer 1 (*SalI*) and 2 (*EcoRI*; see Extended
210 Data Tab. 2). The *SalI*/*EcoRI* digested PCR product was ligated into a double-digested pUC18
211 cloning vector and propagated as pUC18-3'-*petD*-5' in NEB 5-alpha *E. coli* cells using ampicillin
212 selection. In the next step, the aminoglycoside adenyl transferase (aadA) spectinomycin
213 resistance cassette [38] was amplified from a pUC18-aadA vector using primers 3 and 4, each
214 containing a *SpeI* restriction site. The cloned *petD/trnR1* region contains a single *SpeI* site into
215 which the aadA cassette was cloned. To do so, intermediate vectors were created. First (pUC18-
216 int1), the *SalI/SpeI* fragment from pUC18-3'-*petD*-5' (1.46 kb) was ligated with the *SpeI* digested
217 aadA PCR fragment, followed by PCR (primers 1 and 5) and blunt ligation of the ~3 kb product
218 into *SmaI* digested empty pUC18 vector. Second (pUC18-int2), the *EcoRI/SpeI* fragment from
219 pUC18-3'-*petD*-5' (0.51 kb) was ligated with the *SpeI* digested aadA PCR fragment, followed by
220 PCR (primers 2 and 6), *XmaI*/*EcoRI* digest of the ~2 kb product, and ligation into an empty
221 pUC18 vector. The 2.4 kb fragment of *BamHI*/*BlpI* digested pUC18-int1 was ligated with the 3.7
222 kb fragment of *BamHI*/*BlpI* digested pUC18-int2 to yield pUC18-3'-*petD*-aadA-5'

223 **Point Mutation and Truncation Plasmid Construction**

224 To generate T4E and T4A mutation as well as the *petD* truncation ΔN (lacking underlined N-
225 terminal amino acids M<u>SVTKK</u>PD…), primers 8-11 and 13 were phosphorylated. Using pUC18-
226 3'-*petD*-aadA-5' as a template, five independent PCRs were done with the following primers: 1
227 and 8 (I), 1 and 9 (II), 1 and 10 (III), 11 and 12 (IV) and 12 and 13 (V). Ligated PCR fragments I
228 and IV served as templates for the T4E PCR (primers 1 and 12) which was further digested
229 (*PacI*/*SalI*) for ~1.36 kb insert swapping and mutant introduction into pUC18-3'-*petD*-aadA-5'
230 (ligation with ~4.78 kb backbone). In a similar fashion, for T4A PCR (primers 1 and 12) PCR
231 fragments II and IV served as templates. For ΔN PCR (primers 1 and 12), fragments III and V
232 served as templates.
233
234
235 **Biolistic Transformation of WT Strain**

236 Mutant strains were generated through chloroplast transformation using plasmids containing the
237 modified *petD* gene version along with an *aadA* cassette to confer spectinomycin resistance (150
238 µg/ml). The recipient wild-type (WT) strain carries a six-histidine tag at the C-terminus of PetA
239 [20]. Spectinomycin resistant clones were selected and replated several times to obtain homoplastic
240 strains (for sequencing primers, see Extended Data Tab. X).
241

242 **Growth conditions and treatments**

243 Cells were maintained at 50 µmol photons m^{-2} s^{-1} at 23°C on agar plates of Tris-acetate-
244 phosphate (TAP) medium or Tris-minimal medium (TP) in the absence of acetate [39] by bubbling
245 sterile air under a 16-h light/8-h dark regime. For state transition treatment, TAP-grown
246 synchronized cultures were freshly diluted one day before the experiment and, upon harvesting
247 (4000 *g*, 5 min, 23°C), adjusted to 5 µg chlorophyll ml^{-1}. Aliquots were either kept for 45 min in
248 aerobic conditions by shaking in 40 µmol photons m^{-2} s^{-1} light upon adding 10 µM 3-(3,4-
249 Dichlorophenyl)-1,1-dimethylurea (DCMU; State 1), or were given anoxic treatment in the dark
250 using a glucose oxidase/catalase cocktail (State 2) [40]. For proteomic analyses of *stt7* experiments,
251 TAP grown cells were shifted to State 2 conditions for 30 min and samples for phospho-
252 proteomic analyses were collected. The strains were checked for photoautotrophic growth for one
253 week by spotting 20 µl of 1×10^6 cells/ml on TP agar plates at 25°C kept under 40 µmol photons
254 m^{-2} s^{-1} (16 h light/8 h dark) and continuous 500 µmol photons m^{-2} s^{-1}.
255 Liquid TP cultures were harvested for optical spectroscopy and Ficol (20% *w*/*v*) was added to the
256 TP resuspension medium.
257
258 **Biochemical methods**
259 Liquid cultures of WT, T4A, T4E, and ΔN were grown in TAP medium and freshly diluted one
260 day before harvesting. The cells were pelleted and mixed in a buffer containing 0.2 M dichloro-
261 diphenyl-trichloroethane, 0.2 M Na_2CO_3, 10 mM NaF, and protease inhibitors (0.2 mM
262 phenylmethylsulfonyl fluoride, 1 mM benzamidine, 20 mM amino caproic acid) to be analyzed
263 via SDS-PAGE [41]. For heme staining the b_6f was isolated using the standard protocol [42] to
264 analyze their purity via SDS-PAGE. The high-spin hemes were stained in gel using 3,3',5,5'-
265 tetramethylbenzidine [43].
266
267 **Generation of *stt7* mutants with CRISPR-CAS9**
268 Chlamydomonas strain CC-125 (*nit1*; *nit2*; *mt*+) was grown in tris-acetate-phosphate (TAP)
269 media under continuous illumination of 50 µmol photons m^{-2} s^{-1} at 22 °C. Single guide RNAs
270 (sgRNAs) were designed by CHOPCHOP using version 5.6 of the *Chlamydomonas*
271 *reinhardtii* genome, and 5'-CTCCTGTAGACCGCTCAATGCGG was selected as the targeting
272 sequence, and sgRNAs were bought will all accessory parts to make it functional (IDT, USA).
273 Ribonucleic protein (RNP) complexes were prepared by duplexing the sgRNA (23% volume per
274 volume, v/v; IDT) and Cas-9 (19% v/v; IDT) within a duplex buffer (58% v/v; IDT) and
275 incubated at 37°C for 25 to 30 min. After treatment with autolysin for 3 hours without shaking,
276 cells were washed with TAP media supplemented with 40 mM of sucrose, resuspended with the
277 same supplemented media to approximately 2 x 10^8 cells mL^{-1}, and electroporated in the presence

278 of a hygromycin resistance DNA cassette (2 µg mL^{-1}) and the 37°C-incubated RNP mixture.
279 After 10 min at room temperature, cells were resuspended in 10 mL of TAP media supplemented
280 with 40 mM of sucrose and left without shaking overnight in dim light (10-20 µmol photons m^{-}
281 ^{2} s^{-1}) at 22°C. Hygromycin resistant transformants were selected on solid TAP media (2% Agar
282 w/v) containing hygromycin (20 µg mL^{-1}). sgRNA targeted regions were amplified via
283 polymerase chain reaction (PCR) to check for full or partial insertion of the hygromycin
284 resistance cassette at the target site using the following primers: STT7 F/R (STT7F: 5'-
285 GCACGAACCAAGACACACATAG-3'; STT7 R: 5'-GTAGACGATGTCACCGCACTT3')
286 with an annealing temperature of 62.6°C (Extended Data Fig. 6). Impaired accumulation of the
287 STT7 protein was then verified by immunodetection (Agrisera, AS15 3080).
288

289 **Sample preparation for mass spectrometry**

290 Protein isolation from cell pellets was carried out as described [37]. Reduction/alkylation of
291 cysteines and tryptic digestion of proteins (100 µg per sample) was performed following the SP4
292 protocol [44] . After digestion, peptides were desalted using PurePep H50 SPE Spin columns
293 (Affinisep). The peptide samples were divided into two aliquots: 5 µg for whole proteome
294 analysis and 95 µg for phosphopeptide enrichment. Both aliquots were dried using vacuum
295 centrifugation before further processing.

296 To enrich phosphopeptides, titanium dioxide (TiO2) beads with 5 µm particle size (Titansphere,
297 GL Sciences) in a metal oxide affinity chromatography (MOAC) procedure were used. TiO2 (1
298 mg per sample) was activated once with acetonitrile and equilibrated three times with loading
299 buffer (LB; 80% (v/v) acetonitrile/5% (v/v) TFA/1 M glycolic acid). Loading buffer was added to
300 create a 10% (w/v) TiO2 suspension. Peptide samples were dissolved in 50 µl LB, combined with
301 10 µl TiO2 suspension, and incubated for 30 minutes at 25°C in an Eppendorf Thermomixer at
302 1,200 rpm). The mixture was transferred to SDB-XC STAGE tips prepared in-house [45]. Unless
303 stated otherwise, all subsequent washing and elution steps were performed using 60 µl buffer
304 volumes with in-between centrifugation at 2000 × g at room temperature. The buffer was
305 removed by centrifugation and the TiO2 beads were washed twice with LB and once with 1%
306 (v/v) acetonitrile/0.1% (v/v) TFA (W1). Non-phosphorylated peptides that were removed from
307 the beads and subsequently bound to the SDB-XC membrane plug were removed by one wash
308 with 80% (v/v) acetonitrile/0.1% (v/v) TFA (W2). The phosphopeptides were eluted from the
309 TiO2 beads onto the SDB-XC material using 160 µl of pH 11 buffer (0.4 M sodium hydrogen
310 phosphate/NaOH with 1% acetonitrile). After washing once with 1% acetonitrile/0.1% TFA, the
311 phosphopeptides were sequentially eluted in three fractions using increasing concentrations of
312 acetonitrile (7.5%, 20%, and 60%) in 100 mM ammonium formate (pH10). For samples from the
313 STT7 experiment, only one fraction (60% acetonitrile in 100 mM ammonium formate (pH10))

314 was collected. The strongly bound phosphopeptides were eluted in two steps: first from the TiO2
315 beads using 5% ammonia, then from the SDB-CX membrane using 60% acetonitrile in 100 mM
316 ammonium formate at pH 10. All fractions were dried by vacuum centrifugation and stored
317 at -80°C until MS analysis.
318

319 **Mass spectrometry**

320 Whole proteome analysis

321 Dried peptide samples were reconstituted in 5 µl of 2% (v/v) acetonitrile/0.05% (v/v) TFA in
322 LC/MS grade water. Samples were analyzed on an LC-MS/MS system consisting of an Ultimate
323 3000 NanoLC (Thermo Fisher Scientific) coupled via a Nanospray Flex ion source (Thermo
324 Fisher Scientific) to a Q Exactive Plus mass spectrometer (Thermo Fisher Scientific). Peptides
325 were concentrated on a trap column (Acclaim Pepmap C18, 5 × 0.3 mm, 3 µm particle size,
326 Thermo Scientific) for 3 min using 4% (v/v) acetonitrile/0.05% (v/v) in LC/MS grade water at a
327 flow rate of 10 µl/min. The trap column was operated in back-flush mode, allowing the transfer
328 of peptides on a reversed-phase column (PepSep Fifty, 500 × 0.075 mm, 1.9 µm particle size,
329 Bruker) for chromatographic separation. The eluents used were 0.1% (v/v) formic acid in LC/MS
330 grade water (A) and 0.1% (v/v) formic acid/80% (v/v) acetonitrile in LC/MS grade water (B).
331 The gradient was programmed as follows: 2.5% to 5% B over 5 min, 5% to 17.5% B over 47
332 min, 17.5% to 40% B over 105 min, 40% to 99% B over 10 min, and 99% B for 20 min. Flow
333 rate was 250 nl/min. The mass spectrometer was operated in data-dependent acquisition (DDA)
334 mod, alternating between one MS1 full scan and up to 12 MS2 scans. Full scans were acquired
335 with the following settings: AGC target 3e6, MS1 resolution 70000, maximum injection time 50
336 ms, scan range: 350–1400 m/z. Settings for MS were: AGC target 5e4, resolution 17500, MS2
337 maximum injection time 80 ms, intensity threshold 1e4, normalized collision energy 27 (HCD)).
338 Dynamic exclusion was set to 'auto', assuming a chromatographic peak width (FWHM) of 60 s.
339

340 **Phosphoproteomic analysis**

341 Prior to analysis, dried peptide samples were reconstituted in 5 µl of 2% (v/v) acetonitrile/0.05%
342 (v/v) TFA in LC/MS grade water. LC-MS/MS system, flow rate and eluent compositions were
343 the same as described above. The gradient for peptide separation was as follows: 2.5% to 5% B
344 over 5 min, 5% to 40% B over 92 min, 40% to 99% B over 10 min, and 99% B for 20 min.

345 The mass spectrometer used the same DDA mode settings as the whole proteome analysis, with
346 two changes: MS2 maximum injection time was increased to 120 ms, and dynamic exclusion was
347 set to 45 s.
348

349 **MS data analysis**

350 For quantitative phosphoproteome analysis, mass spectrometry raw data from nonenriched and
351 enriched samples were searched using Fragpipe [46,47] against a concatenated, non-redundant
352 database containing *Chlamydomonas reinhardtii* protein sequences from v5.6 and v6.1 gene
353 models (Phytozome 13, phytozome-next.jgi.doe.gov). In addition, the polypeptide sequences of
354 mutated/tagged proteins were added to the database. Default 'LFQ-MBR' workflow settings were
355 applied to data from whole proteome samples, while the 'LFQ-phospho' workflow was used for
356 phosphopeptide samples. A false discovery rate of 1% was applied at both peptide and protein
357 levels.

358 Fragpipe output files containing peptide/protein identifications and quantitative data
359 ('combined_modified_peptide.tsv' from enriched samples and 'combined_protein.tsv' from whole
360 proteome samples) were reformatted using a custom Python script to ensure compatibility with
361 Phospho-Analyst (v. 1.0.2), which was used for differential expression analysis [48]: Missing
362 values were imputed using the 'MinProb' function, and variance stabilizing transformation was
363 applied to normalize phosphosite intensities. Since the whole proteome LFQ data was already
364 normalized in Fragpipe, no additional normalization steps were needed. Phospho-Analyst
365 automatically corrected phosphosite abundance changes for underlying protein levels. A
366 phosphorylation site localization probability threshold of 0.33 was applied, and p-values were
367 adjusted using the Benjamini-Hochberg method. Predicted protein localizations are based on
368 recently published data (PB-Chlamy)[49].

369 The mass spectrometry proteomics data have been deposited to the ProteomeXchange
370 Consortium (http://proteomecentral.proteomexchange.org) via the PRIDE partner repository [50]
371 with the dataset identifier PXD060640.

372

373 **Optical spectroscopy**

374 The flash-induced b_6f measurements were carried out by using a Joliot-type spectrophotometer
375 (JTS-150, SpectroLogiX) equipped with the interference filters and deconvolution procedures as
376 reported previously [3]. Cells were adapted to alternating 7.5 s darkness and 5 s actinic light (AL;
377 550 µmol photons m^{-2} s^{-1} peaking at 630 nm). Sub-saturating 6-ns flashes (Q-switched Nd:YAG,
378 Continuum) were fired at 3 s darkness, hitting ~40% of PSI. Three averaged baseline spectra (in
379 the absence of a flash) were subtracted from each flash measurement at the b_6f-specific
380 wavelengths. For multiple turnover conditions, previously described conditions and protocols
381 used cells which were adapted to alternating 2.5 s AL and dark. Briefly, ETR were obtained in
382 the presence of LEF but referred to PSI charge separation activity. This stems from separate ECS
383 calibration measurements that allowed, via saturating single-turnover flashes, for the conversion

of optical changes (obtained as $\Delta I/I$ at 520 nm - 546nm) into the ECS signals corresponding to 1 PSI charge separation [51]. The ETR protocol was based on a Dark Interval Relaxation Kinetics approach [52,53]. P700 measurements during 2.5 s AL and dark relied on the Klughammer & Schreiber method [54].

References

1 Malone, L. A., Proctor, M. S., Hitchcock, A., Hunter, C. N. & Johnson, M. P. Cytochrome b(6)f - Orchestrator of photosynthetic electron transfer. *Biochim Biophys Acta Bioenerg* **1862**, 148380 (2021). https://doi.org:10.1016/j.bbabio.2021.148380

2 Mitchell, P. The protonmotive Q cycle: a general formulation. *FEBS Lett* **59**, 137-139 (1975). https://doi.org:10.1016/0014-5793(75)80359-0

3 Buchert, F., Mosebach, L., Gabelein, P. & Hippler, M. PGR5 is required for efficient Q cycle in the cytochrome b6f complex during cyclic electron flow. *Biochem J* **477**, 1631-1650 (2020). https://doi.org:10.1042/BCJ20190914

4 Rumberg, B. & Siggel, U. Ph Changes in Inner Phase of Thylakoids during Photosynthesis. *Naturwissenschaften* **56**, 130-+ (1969). https://doi.org:Doi 10.1007/Bf00601025

5 Nishio, J. N. & Whitmarsh, J. Dissipation of the Proton Electrochemical Potential in Intact Chloroplasts (II. The pH Gradient Monitored by Cytochrome f Reduction Kinetics). *Plant Physiol* **101**, 89-96 (1993).

6 Li, X. P. *et al.* A pigment-binding protein essential for regulation of photosynthetic light harvesting. *Nature* **403**, 391-395 (2000).

7 Peers, G. *et al.* An ancient light-harvesting protein is critical for the regulation of algal photosynthesis. *Nature* **462**, 518-521 (2009). https://doi.org:10.1038/nature08587

8 Girolomoni, L. *et al.* LHCSR3 is a nonphotochemical quencher of both photosystems in. *P Natl Acad Sci USA* **116**, 4212-4217 (2019). https://doi.org:10.1073/pnas.1809812116

9 Allorent, G. *et al.* A dual strategy to cope with high light in Chlamydomonas reinhardtii. *Plant Cell* **25**, 545-557 (2013). https://doi.org:10.1105/tpc.112.108274

10 Depege, N., Bellafiore, S. & Rochaix, J. D. Role of chloroplast protein kinase Stt7 in LHCII phosphorylation and state transition in Chlamydomonas. *Science* **299**, 1572-1575 (2003). https://doi.org:10.1126/science.1081397

11 Rochaix, J. D. Regulation and dynamics of the light-harvesting system. *Annu Rev Plant Biol* **65**, 287-309 (2014). https://doi.org:10.1146/annurev-arplant-050213-040226

12 Cariti, F. *et al.* Regulation of Light Harvesting in Chlamydomonas reinhardtii Two Protein Phosphatases Are Involved in State Transitions. *Plant Physiol* **183**, 1749-1764 (2020). https://doi.org:10.1104/pp.20.00384

13 Lemeille, S. *et al.* Analysis of the chloroplast protein kinase Stt7 during state transitions. *PLoS Biol* **7**, e45 (2009). https://doi.org:10.1371/journal.pbio.1000045

14 Shapiguzov, A. *et al.* Activation of the Stt7/STN7 Kinase through Dynamic Interactions with the Cytochrome b_6f Complex. *Plant Physiol* **171**, 82-92 (2016). https://doi.org:10.1104/pp.15.01893

15 Singh, S. K. *et al.* Trans-membrane signaling in photosynthetic state transitions: Redox- and structure-dependent interaction *in vitro* between STT7 kinase and the cytochrome b_6f complex. *J Biol Chem* **291**, 21740-21750 (2016). https://doi.org:10.1074/jbc.M116.732545

16 Wu, J. *et al.* Functional redox links between Lumen Thiol Oxidoreductase1 and Serine/Threonine-protein kinase STN7. *Plant Physiol* (2021). https://doi.org:10.1093/plphys/kiab091

17 Dumas, L. *et al.* A stromal region of cytochrome b_6f subunit IV is involved in the activation of the Stt7 kinase in *Chlamydomonas*. *Proc Natl Acad Sci U S A* **114**, 12063-12068 (2017). https://doi.org:10.1073/pnas.1713343114

18 Riche, A. *et al.* The stromal side of the cytochrome b6f complex regulates state transitions. *Plant Cell* **36**, 4234-4244 (2024). https://doi.org:10.1093/plcell/koae190

19 Bergner, S. V. *et al.* STATE TRANSITION7-dependent phosphorylation is modulated by changing environmental conditions, and its absence triggers remodeling of photosynthetic protein complexes. *Plant Physiol* **168**, 615-634 (2015). https://doi.org:10.1104/pp.15.00072

20 Choquet, Y., Zito, F., Wostrikoff, K. & Wollman, F. A. Cytochrome *f* translation in *Chlamydomonas* chloroplast is autoregulated by its carboxyl-terminal domain. *Plant Cell* **15**, 1443-1454 (2003).

21 Takahashi, H. *et al.* PETO Interacts with Other Effectors of Cyclic Electron Flow in *Chlamydomonas*. *Mol Plant* **9**, 558-568 (2016). https://doi.org:10.1016/j.molp.2015.12.017

22 Dinc, E. *et al.* LHCSR1 induces a fast and reversible pH-dependent fluorescence quenching in LHCII in Chlamydomonas reinhardtii cells. *Proc Natl Acad Sci U S A* **113**, 7673-7678 (2016). https://doi.org:10.1073/pnas.1605380113

23 Wollman, F.-A. & Lemaire, C. Studies on kinase-controlled state transitions in Photosystem II and b_6f mutants from *Chlamydomonas reinhardtii* which lack quinone-binding proteins. *Biochimica et Biophysica Acta (BBA) - Bioenergetics* **933**, 85-94 (1988). https://doi.org:https://doi.org/10.1016/0005-2728(88)90058-8

24 Wollman, F.-A. & Bennoun, P. A new chlorophyll-protein complex related to Photosystem I in *Chlamydomonas reinhardtii*. *Biochim Biophys Acta* **680**, 352-360 (1982).

25 Pfalz, J., Liere, K., Kandlbinder, A., Dietz, K. J. & Oelmuller, R. pTAC2, -6, and -12 are components of the transcriptionally active plastid chromosome that are required for plastid gene expression. *Plant Cell* **18**, 176-197 (2006). https://doi.org:10.1105/tpc.105.036392

26 Ingelsson, B. & Vener, A. V. Phosphoproteomics of Arabidopsis chloroplasts reveals involvement of the STN7 kinase in phosphorylation of nucleoid protein pTAC16. *FEBS Lett* **586**, 1265-1271 (2012). https://doi.org:10.1016/j.febslet.2012.03.061

27 Scholz, M. *et al.* Light-dependent N-terminal phosphorylation of LHCSR3 and LHCB4 are interlinked in *Chlamydomonas reinhardtii*. *Plant J* **99**, 877-894 (2019). https://doi.org:10.1111/tpj.14368

28 Lemeille, S., Turkina, M. V., Vener, A. V. & Rochaix, J. D. Stt7-dependent phosphorylation during state transitions in the green alga Chlamydomonas reinhardtii. *Molecular & cellular proteomics : MCP* **9**, 1281-1295 (2010). https://doi.org:10.1074/mcp.M000020-MCP201

29 Pan, X. *et al.* Structural basis of LhcbM5-mediated state transitions in green algae. *Nat Plants* **7**, 1119-1131 (2021). https://doi.org:10.1038/s41477-021-00960-8

30 Alric, J., Pierre, Y., Picot, D., Lavergne, J. & Rappaport, F. Spectral and redox characterization of the heme c_i of the cytochrome b_6f complex. *Proc Natl Acad Sci U S A* **102**, 15860-15865 (2005). https://doi.org:10.1073/pnas.0508102102

31 Buchert, F., Scholz, M. & Hippler, M. Electron transfer via cytochrome b_6f complex displays sensitivity to antimycin A upon STT7 kinase activation. *Biochem J* **479**, 111-127 (2022). https://doi.org:10.1042/BCJ20210802

32 Valkova-Valchanova, M., Darrouzet, E., Moomaw, C. R., Slaughter, C. A. & Daldal, F. Proteolytic Cleavage of the Fe−S Subunit Hinge Region of Rhodobacter capsulatus bc1 Complex: Effects of Inhibitors and Mutations. *Biochemistry* **39**, 15484-15492 (2000). https://doi.org:10.1021/bi000751d

33 Cooley, J. W., Lee, D.-W. & Daldal, F. Across Membrane Communication between the Qo and Qi Active Sites of Cytochrome bc1. *Biochemistry* **48**, 1888-1899 (2009). https://doi.org:10.1021/bi802216h

34 Pintscher, S. *et al.* Molecular basis of plastoquinone reduction in plant cytochrome b(6)f. *Nat Plants* (2024). https://doi.org:10.1038/s41477-024-01804-x

35 Zito, F. *et al.* The Qo site of cytochrome b_6f complexes controls the activation of the LHCII kinase. *EMBO J* **18**, 2961-2969 (1999). https://doi.org:10.1093/emboj/18.11.2961

36 Mekala, N. R., Suorsa, M., Rantala, M., Aro, E. M. & Tikkanen, M. Plants Actively Avoid State Transitions upon Changes in Light Intensity: Role of Light-Harvesting Complex II Protein Dephosphorylation in High Light. *Plant physiology* **168**, 721-734 (2015). https://doi.org:10.1104/pp.15.00488

37 Younas, M., Scholz, M., Marchetti, G. M. & Hippler, M. Remodeling of algal photosystem I through phosphorylation. *Biosci Rep* **43** (2023). https://doi.org:10.1042/BSR20220369

38 Fu, H. Y. *et al.* Redesigning the Q(A) binding site of Photosystem II allows reduction of exogenous quinones. *Nat Commun* **8**, 15274 (2017). https://doi.org:10.1038/ncomms15274

39 Gorman, D. S. & Levine, R. P. Cytochrome *f* and plastocyanin: their sequence in the photosynthetic electron transport chain of *Chlamydomonas reinhardtii*. *Proc Natl Acad Sci U S A* **54**, 1665-1669 (1965).

40 Buchert, F., Mosebach, L., Gäbelein, P. & Hippler, M. PGR5 is required for efficient Q cycle in the cytochrome b_6f complex during cyclic electron flow. *Biochemical Journal* **477**, 1631-1650 (2020). https://doi.org:10.1042/bcj20190914

41 Schägger, H. & Von Jagow, G. Tricine-sodium dodecyl sulfate-polyacrylamide gel electrophoresis for the separation of proteins in the range from 1 to 100 kDa. *Analytical biochemistry* **166**, 368-379 (1987).

42 Stroebel, D., Choquet, Y., Popot, J. L. & Picot, D. An atypical haem in the cytochrome b_6f complex. *Nature* **426**, 413-418 (2003). https://doi.org:10.1038/nature02155

43 Thomas, P. E., Ryan, D. & Levin, W. An improved staining procedure for the detection of the peroxidase activity of cytochrome P-450 on sodium dodecyl sulfate polyacrylamide gels. *Anal Biochem* **75**, 168-176 (1976). https://doi.org:10.1016/0003-2697(76)90067-1

44 Johnston, H. E. *et al.* Solvent Precipitation SP3 (SP4) Enhances Recovery for Proteomics Sample Preparation without Magnetic Beads. *Anal Chem* **94**, 10320-10328 (2022). https://doi.org:10.1021/acs.analchem.1c04200

45 Rappsilber, J., Mann, M. & Ishihama, Y. Protocol for micro-purification, enrichment, pre-fractionation and storage of peptides for proteomics using StageTips. *Nature Protocols* **2**, 1896-1906 (2007). https://doi.org:10.1038/nprot.2007.261

46 Kong, A. T., Leprevost, F. V., Avtonomov, D. M., Mellacheruvu, D. & Nesvizhskii, A. I. MSFragger: ultrafast and comprehensive peptide identification in mass spectrometry–

based proteomics. *Nature Methods* **14**, 513-520 (2017). https://doi.org:10.1038/nmeth.4256

47 Yu, F. *et al.* Analysis of DIA proteomics data using MSFragger-DIA and FragPipe computational platform. *Nat Commun* **14**, 4154 (2023). https://doi.org:10.1038/s41467-023-39869-5

48 Zhang, H. *et al.* Phospho-Analyst: An Interactive, Easy-to-Use Web Platform To Analyze Quantitative Phosphoproteomics Data. *J Proteome Res* **22**, 2890-2899 (2023). https://doi.org:10.1021/acs.jproteome.3c00186

49 Wang, L. *et al.* A chloroplast protein atlas reveals punctate structures and spatial organization of biosynthetic pathways. *Cell* **186**, 3499-3518.e3414 (2023). https://doi.org:https://doi.org/10.1016/j.cell.2023.06.008

50 Perez-Riverol, Y. *et al.* The PRIDE database and related tools and resources in 2019: improving support for quantification data. *Nucleic acids research* **47**, D442-D450 (2019).

51 Bailleul, B., Cardol, P., Breyton, C. & Finazzi, G. Electrochromism: a useful probe to study algal photosynthesis. *Photosynthesis Research* **106**, 179-189 (2010). https://doi.org:10.1007/s11120-010-9579-z

52 Sacksteder, C. A. & Kramer, D. M. Dark-interval relaxation kinetics (DIRK) of absorbance changes as a quantitative probe of steady-state electron transfer. *Photosynth Res* **66**, 145 (2000). https://doi.org:10.1023/a:1010785912271

53 Joliot, P. & Joliot, A. Cyclic electron transfer in plant leaf. *Proc Natl Acad Sci U S A* **99**, 10209-10214 (2002).

54 Klughammer, C. & Schreiber, U. An improved method, using saturating light-pulses, for the determination of photosystem-I quantum yield via $P700^{+}$-absorbance changes at 830nm. *Planta* **192**, 261-268 (1994).

Acknowledgements

M.H. (507704013) and F. B. (507704013) acknowledge funding by the Deutsche Forschungsgemeinschaft (DFG FOR 5573/1). M.H. acknowledges the RECTOR program in association with the University of Okayama, Japan. F. B. acknowledges Deutsche Forschungsgemeinschaft 461765884. Y.M. acknowledges the Alexander von Humboldt Foundation for a Research Fellowship for postdocs (1219125). A.B. acknowledges the support of Carnegie Science.

Author contributions

M.H. and F.B. designed the project. A.Z. and F.B. did genetic engineering and kinetic measurements and analyses. S.B. contributed to mutant analyses. C.S. and A.B. produced the *stt7* KO strains. M.S. did the mass spectrometric measurements and data evaluation. M.S. and M.H. analysed the mass spectrometric data. M.H wrote the manuscript with contributions from F.B., A.Z., A.B. and M.S. All authors contributed to the analysis and the final version of the manuscript.

Competing interests

The authors declare no competing interests.

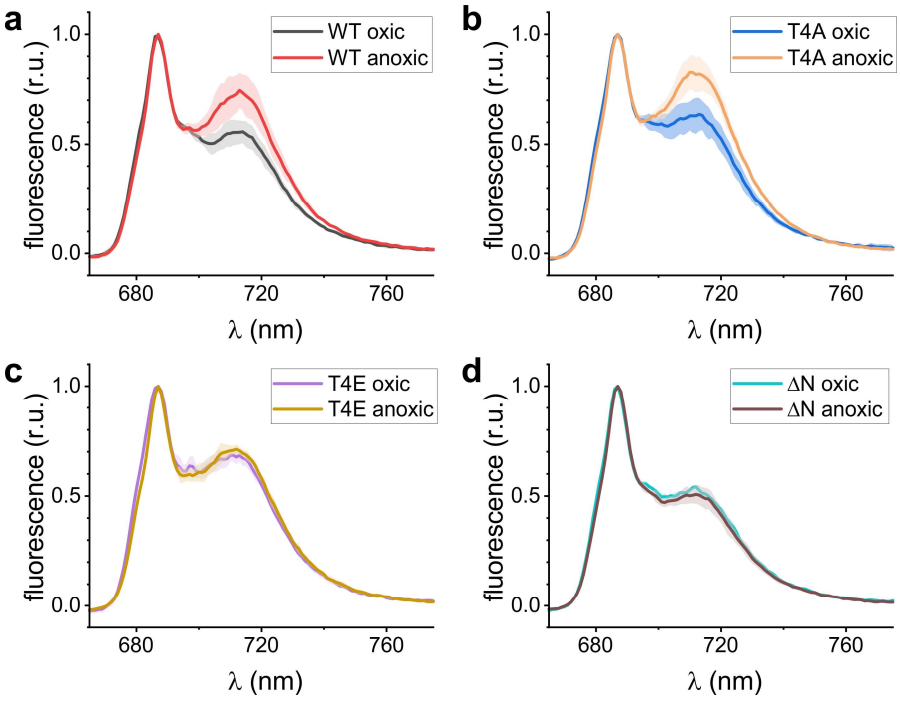

Fig. 1. The relative antenna cross section is shown via chlorophyll fluorescence emission spectra at 77 K. These spectra were averaged (N = 3 ± SD) and normalized to photosystem II-attached antenna emission signals at ~687 nm. Panels a – d highlight the differences in antenna attached to photosystem I under State 1 (oxic) and State 2 (anoxic), contributing to ~712 nm emissions.

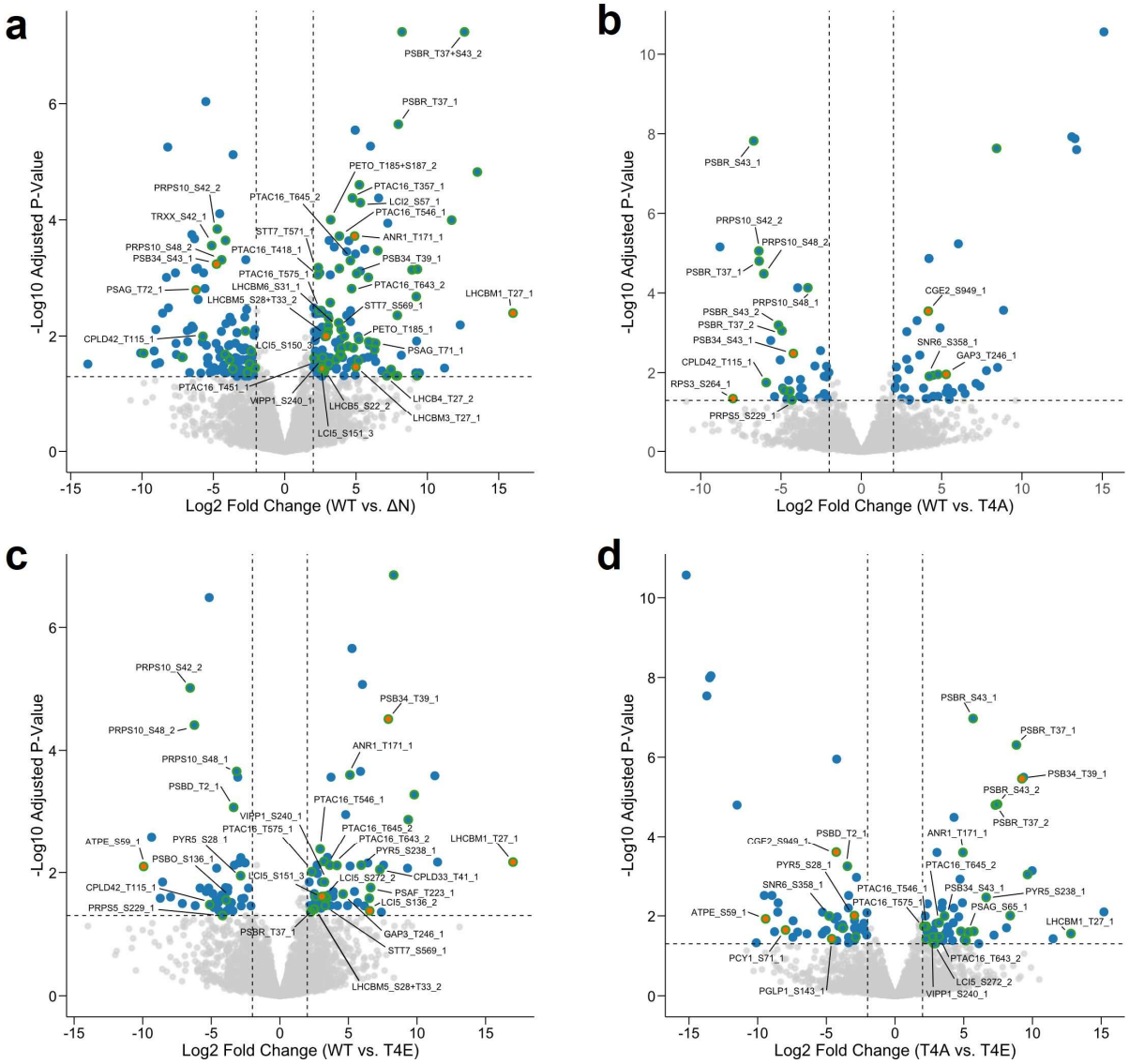

Fig. 2. Volcano plots visualizing effect of PetD mutations on protein phosphorylation. Phosphorylation sites with FDR-adjusted p-value < 0.05 and |$\log_2$ fold change| > 2 are highlighted in blue, with threshold boundaries shown as dashed lines. Data points are shown in orange instead of blue when all values for one strain in the fold-change calculation are imputed due to completely missing data. Green halos indicate chloroplast-encoded proteins and nuclear-encoded proteins with confirmed or predicted (PB-Chlamy) chloroplast localization. Phosphorylation $\log_2$ fold changes are normalized to corresponding protein abundance levels to account for changes in protein expression. Numbers at he end of data labels indicate peptide multiplicity (total phosphorylations per peptide, e.g. PRPS10_S42_2 = PRPS10 with phosphorylated S42 and one additional phosphorylation on the same peptide). A) WT vs. ΔN. B) WT vs. T4A. C) WT vs. T4E. D) T4A vs. T4E.

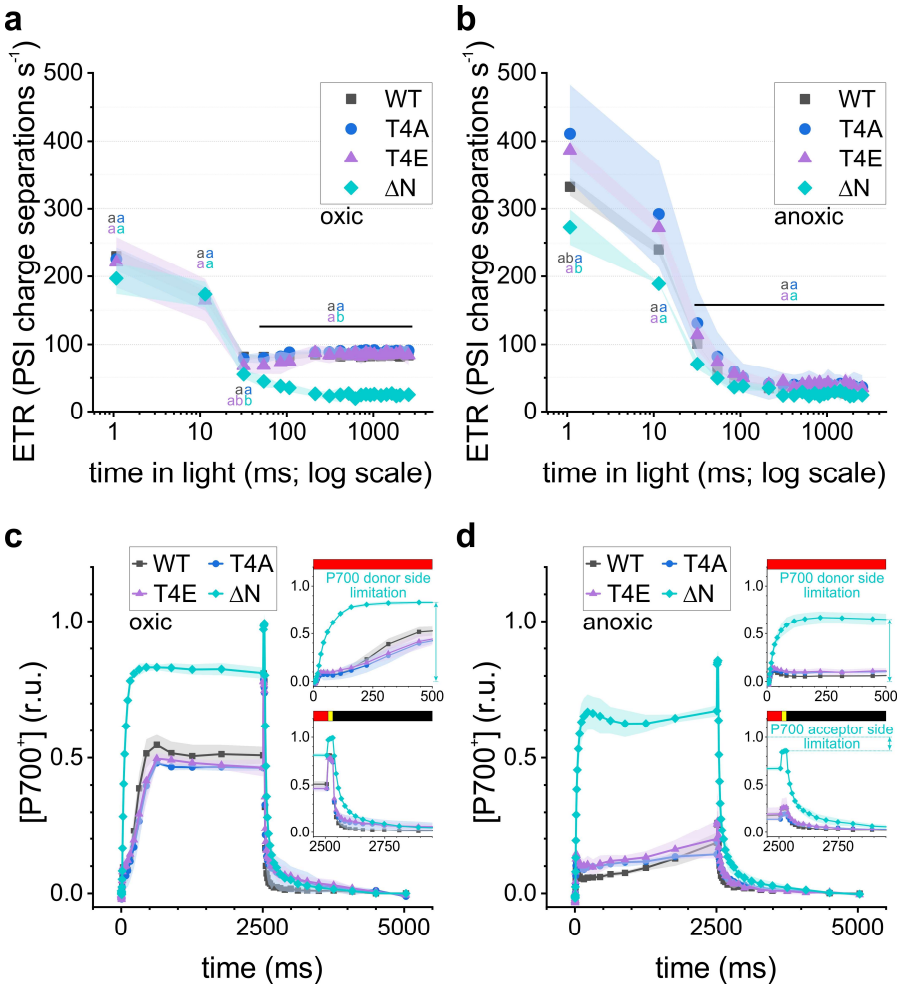

588

589 **Fig. 3. Photosynthetic activities of the cytochrome *b*$_6$*f* variants are shown.** Averaged kinetics
590 are depicted (N = 3 ± SD). **a**, Electron transfer rates (ETR) developed over the 2.5-s illumination
591 period under oxic conditions. The letters at the punctual rates indicate statistical significances (One-
592 Way ANOVA/Tukey-HSD, $P < 0.05$) **b**, ETR developments are shown under anoxic conditions.
593 **c**, Quantification of oxidized primary PSI donor ([P700$^+$]) is plotted under oxic conditions. Red,
594 yellow, and black bar represent actinic light intensities of 550, 3000, and 0 µmol photons m^{-2} s^{-1}.
595 **d**, The P700 kinetics are shown as in panel c but under anoxic conditions.

596

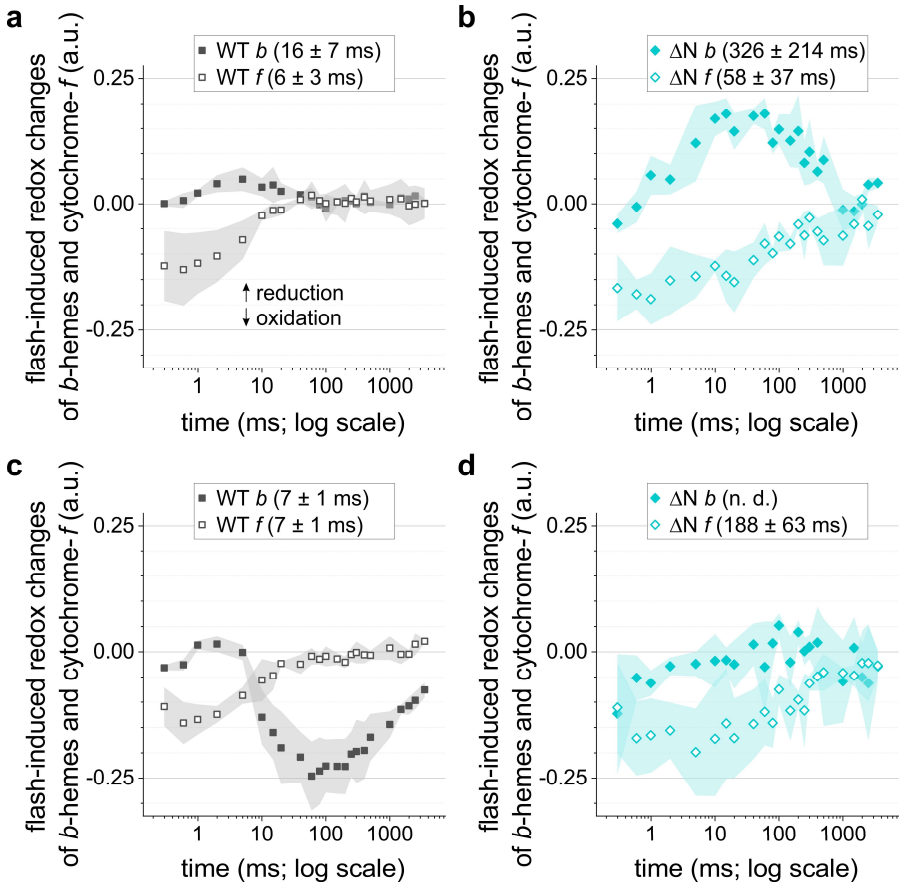

Fig. 4. Single turnover redox changes of the cytochrome b_6f hemes are shown. Averaged kinetics are depicted ($N = 3 \pm$ SD). WT (**a**, **c**) as well as the ΔN mutant (**b**, **d**) were measured under oxic (**a**, **b**) and anoxic conditions (**c**, **d**). The averaged half-times of cytochrome-*f* reduction and *b*-hemes oxidation are given in the panels' legends (n. d.; not determined).

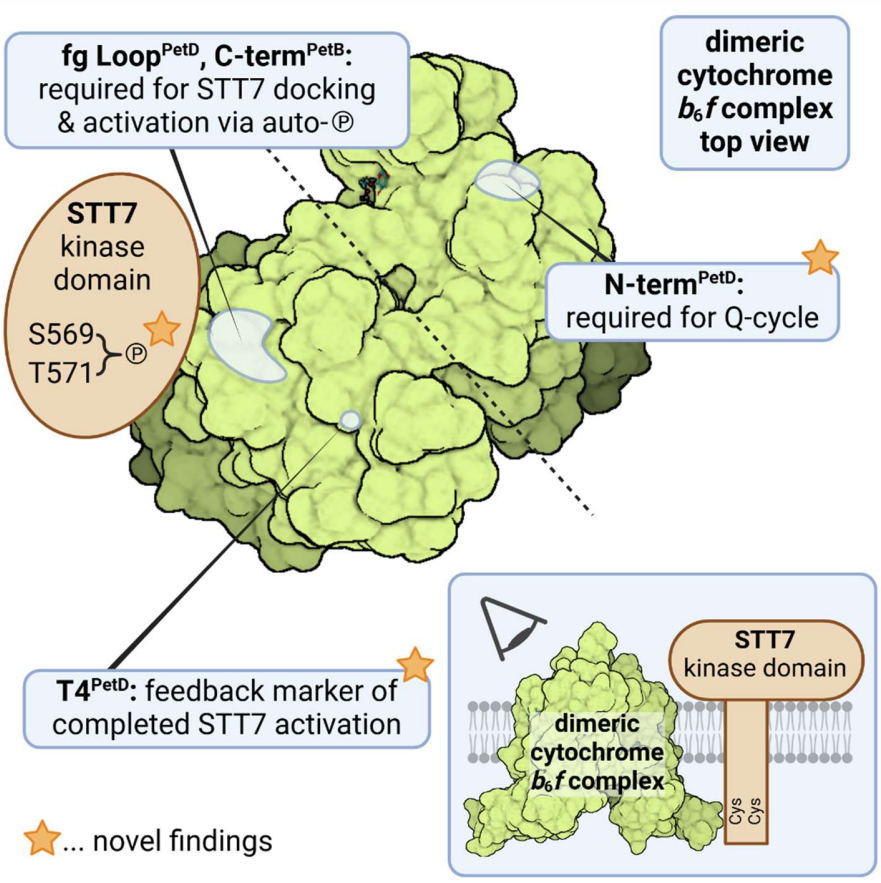

Extended Data Fig. 1. Graphical abstract of the cytochrome b_6f complex interplay with STT7 kinase regulation. The N-terminus of PetD (subunit-IV) has been investigated and the focus was on T4. Previously known processes are included for reference. The drawing was created with Biorender.

608

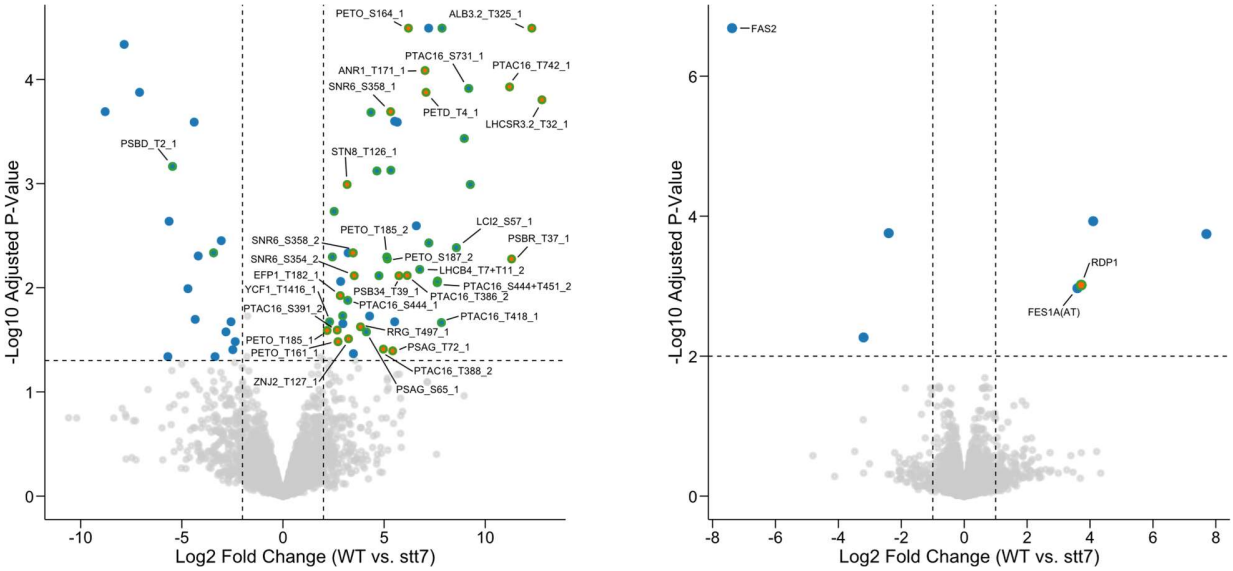

Extended Data Fig. 2. Volcano plots visualizing differential phosphorylation (A) and protein expression (B) between WT and *stt7* mutant. Proteins with FDR-adjusted p-value < 0.01 and $|\log_2$ fold change$|$ > 1 are highlighted in blue, with threshold boundaries shown as dashed lines. Data points are shown in orange instead of blue when all values for one strain in the fold-change calculation are imputed due to completely missing data. Green halos indicate chloroplast-encoded proteins and nuclear-encoded proteins with confirmed or predicted (PB-Chlamy) chloroplast localization.

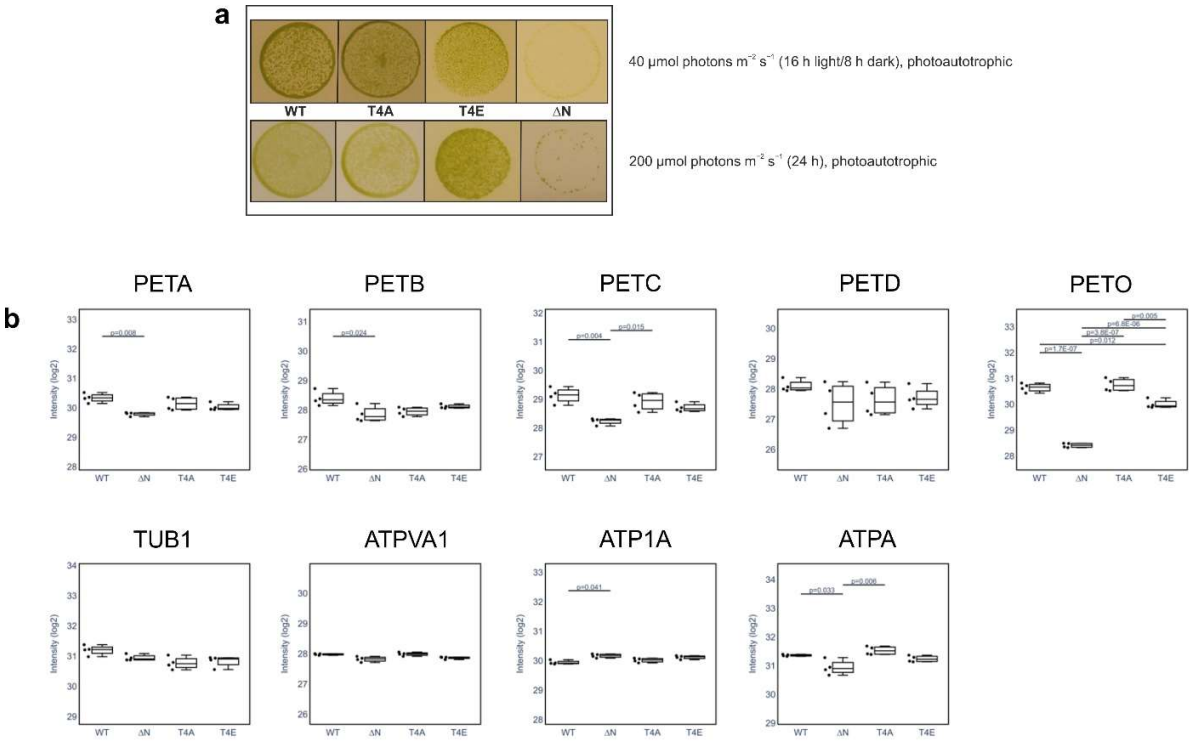

Extended Data Fig. 3. Growth analysis in varying light conditions and protein expression in the mutants. **a**. Spot tests on minimal media compare the growth under two light conditions (40 and 200 µmol photons m^{-2} s^{-1}). **b**. Protein expression of *b6f* subunits in the engineered PetD strains. The box plots visualize the log_2 protein LFQ intensities.

614

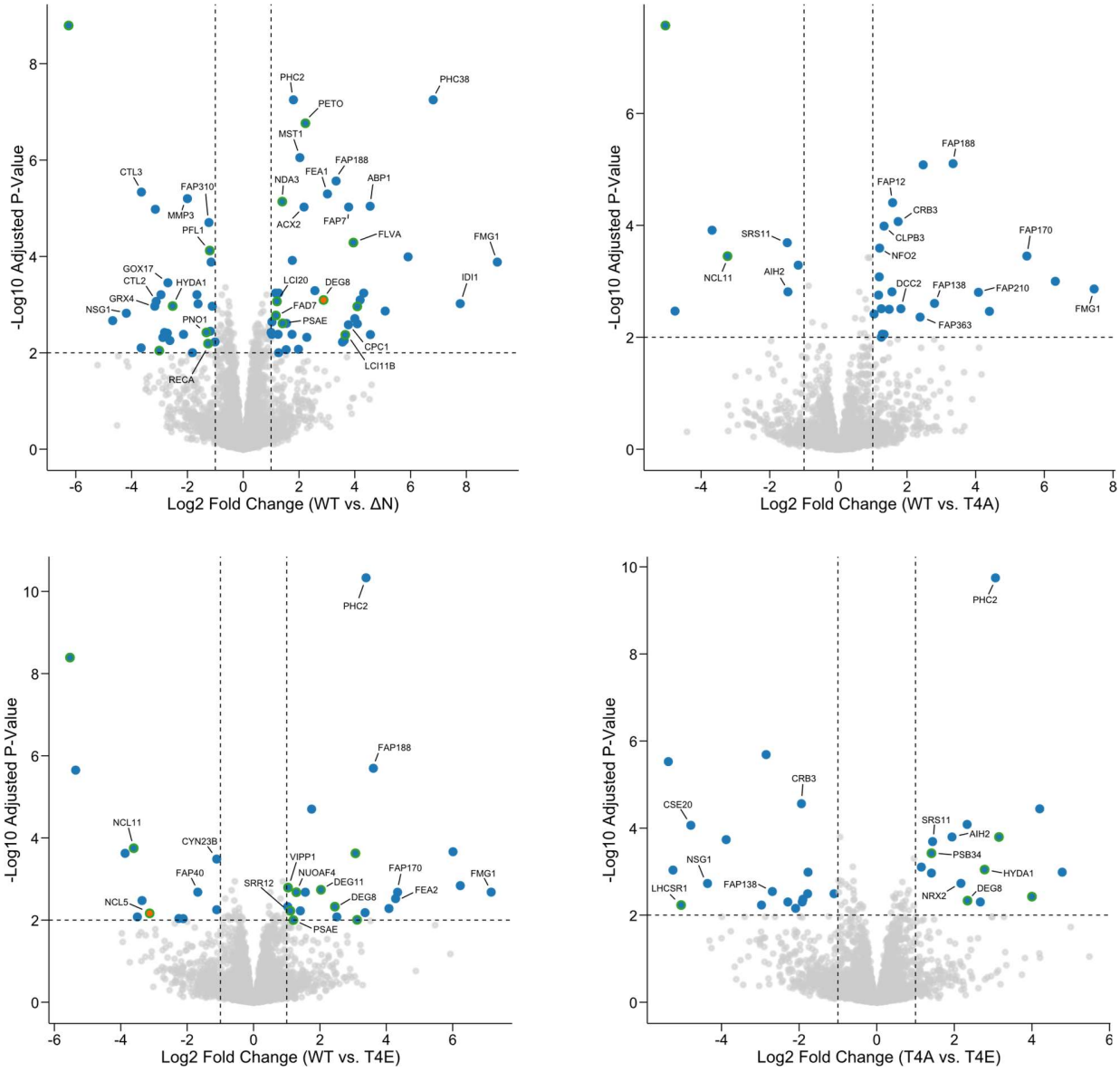

Extended Data Fig. 4. Volcano plots visualizing differential protein expression between WT and PetD mutants. Proteins with FDR-adjusted p-value < 0.01 and $|\log_2$ fold change$|$ > 1 are highlighted in blue, with threshold boundaries shown as dashed lines. Data points are shown in orange instead of blue when all values for one strain in the fold-change calculation are imputed due to completely missing data. Green halos indicate chloroplast-encoded proteins and nuclear-encoded proteins with confirmed or predicted (PB-Chlamy) chloroplast localization. A) WT vs. ΔN. B) WT vs. T4A. C) WT vs. T4E. D) T4A vs. T4E.

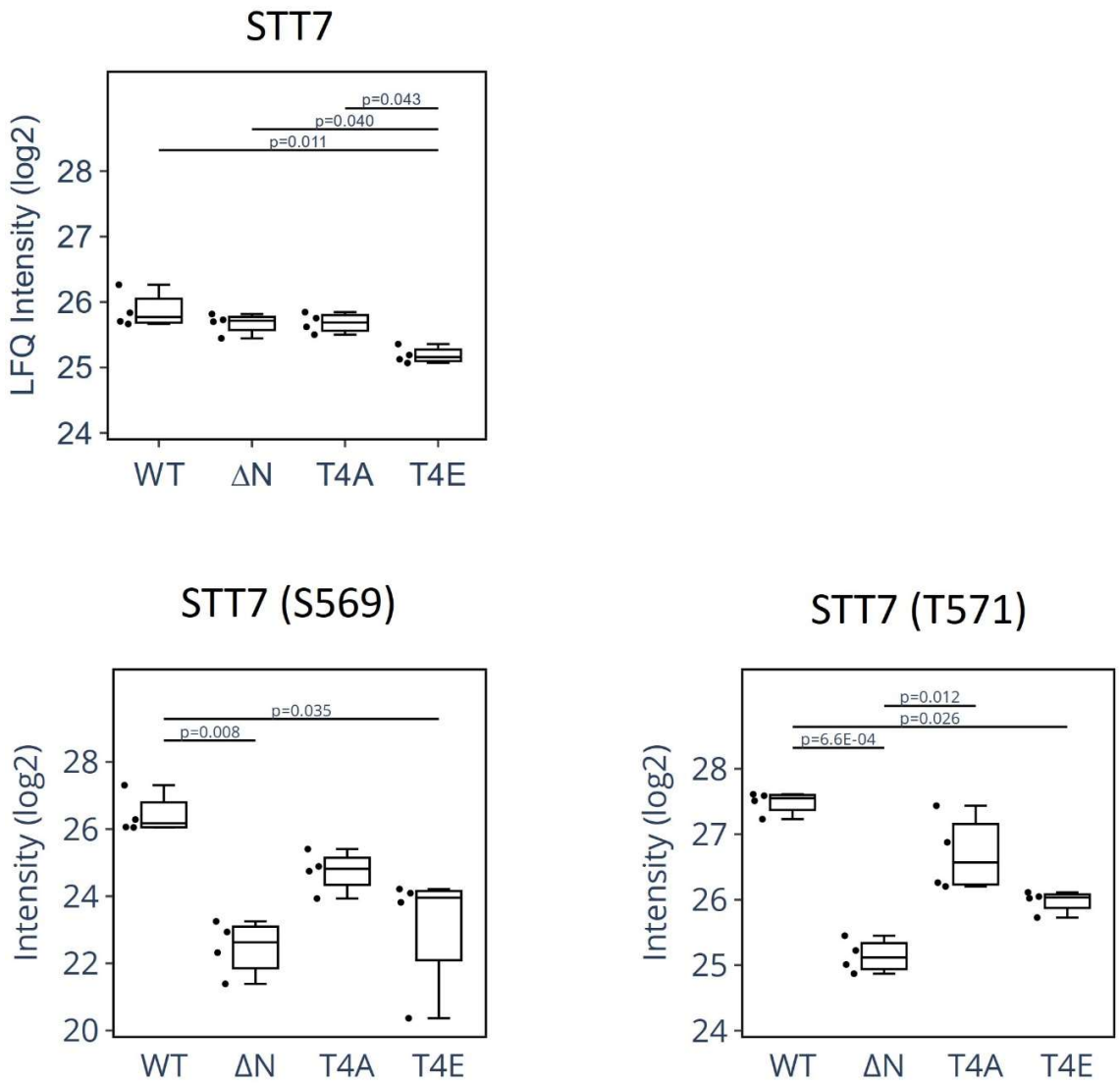

615
616 **Extended Data Fig. 5. STT7 protein expression and selected autophosphorylation amounts**
617 **in the engineered PetD strains.** The box plots visualize $\log_2$ protein LFQ (A) and phosphosite
618 intensities (B+C).
619

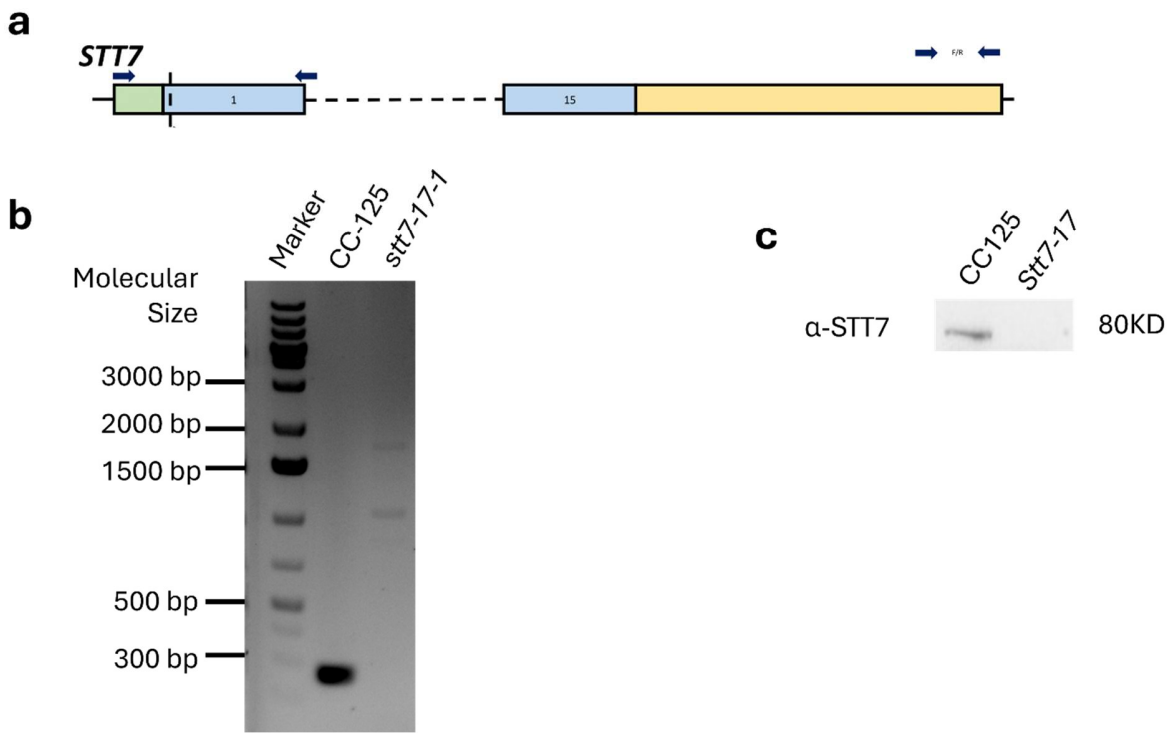

Extended Data Fig. 6. Generation of the *stt7* CRISPR/Cas mutant. a. The gene map of the *STT7* gene showing 5' UTR (green), numbered exons (blue) and 3'UTR (yellow) with predicted cut site (vertical dotted line) and primers used to verify the genotype of the insertion (blue arrows). **b.** Genetic characterization of the *stt7* mutant and its control (CC125) using PCR on genomic DNA. **c.** Immunodetection of STT7 in the *stt7* mutant and its control (CC125).

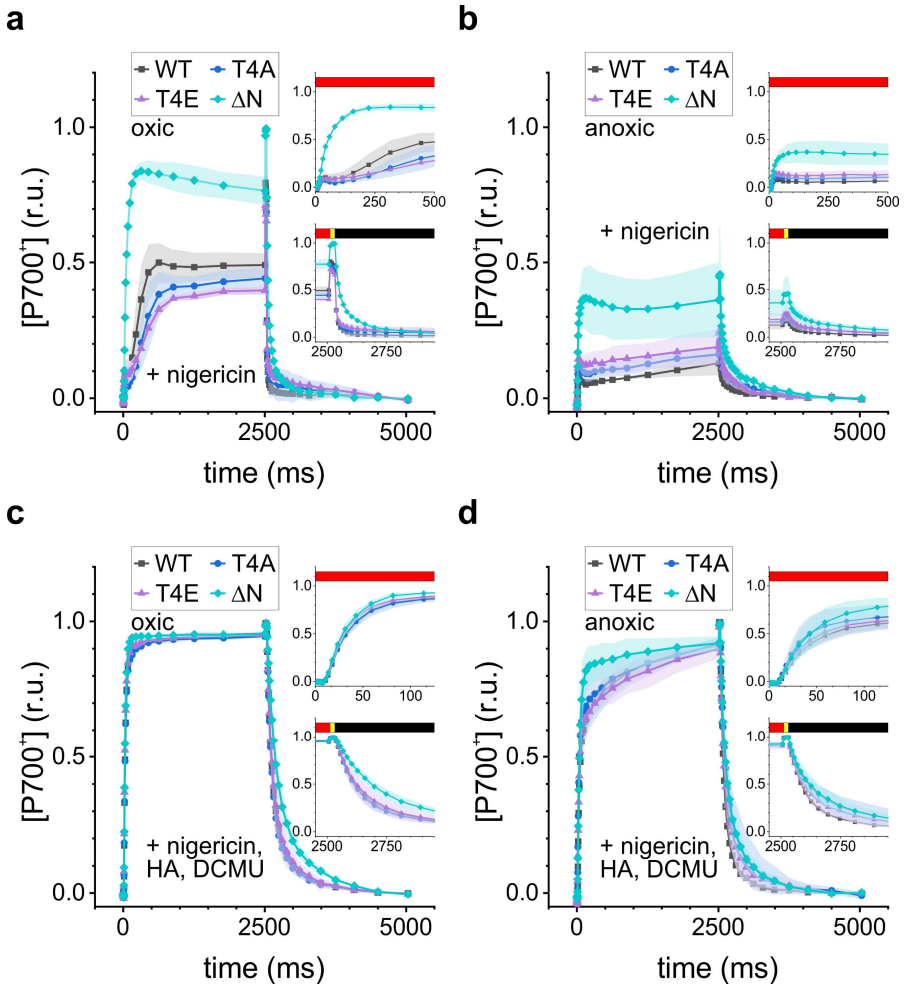

Extended Data Fig. 7. Photosynthetic activities of the cytochrome *b*$_6$*f* variants are shown for P700. Averaged kinetics are depicted (N = 3 ± SD) and the reference measurements are shown in main text Figs. 3c and 3d. The redox changes of primary PSI donor ([P700$^+$]) is plotted (**a**) under oxic and (**b**) anoxic conditions in the presence of 10 µM nigericin, acting as H^+/K^+ exchanger to attenuate ΔpH in favor of an electric field. Red, yellow, and black bar represent actinic light intensities of 550, 3000, and 0 µmol photons m^{-2} s^{-1}. **c**, The conditions were as in panel a but photosystem II was inhibited by hydroxyl amine (HA; 2 mM) and 3-(3,4-Dichlorophenyl)-1,1-dimethylurea (DCMU; 20 µM). **d**, The conditions were as in panel c except for the anoxic pre-treatment.

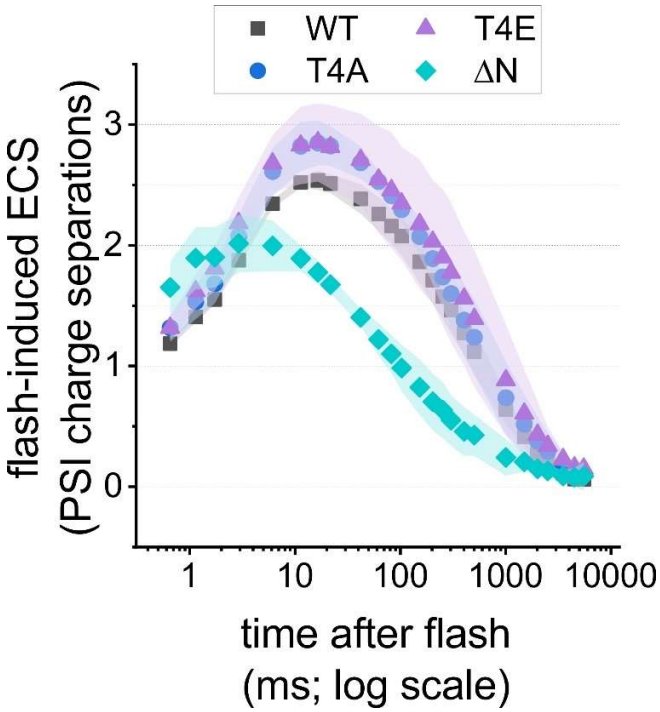

664

665 **Extended Data Fig. 8. Laser flash-induced electrochromic shift (ECS) shows multiphasic**
666 **kinetics that rely on activities of both photosystems, the cytochrome *b*$_6$*f* complex and ATP**
667 **synthase.** Averaged measurements are shown (*N*=3 ± SD).

668

669

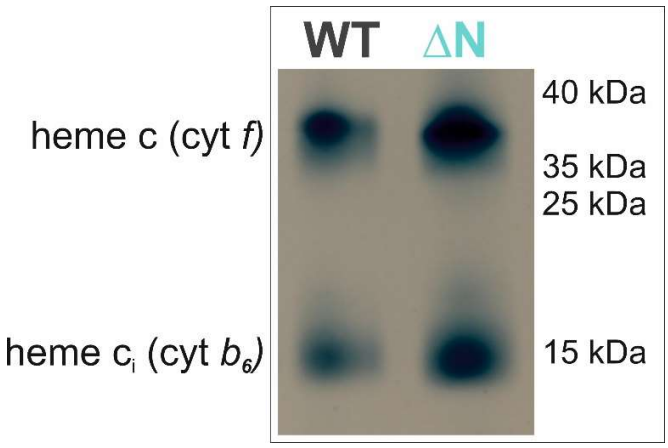

670

671 **Extended Data Fig. 9. Heme staining of isolated *b6f* using the TMBZ method.** Heme c_i was
672 present in the ΔN mutant strain.

673 **Extended Data Tab. 2. List of primers used for plasmid construction and biolistic**
674 **transformation of the chloroplast genome.**
675

Oligo number in text	5'-3' oligo sequence
1	tatagtcgactgccactgacgtcccgtcagg
2	ttaagaattcctgccactgagctcccgtaagg
3	ttaatactagtggatcgcactctaccgattgagttac
4	ccaggactagtcttttacgaatacacatatgg
5	ccaggtctagacttttacgaatacacatatgg
6	ttaatcccgggggatcgcactctaccgattgagttac
7	gtaactcaatcggtagagtgcgatcc
8	caggtttttctcaactgacatatttatttatc
9	caggtttttttgcaactgacatatttatttatc
10	catatttatttatccgttaattttcaataaaac
11	atttaagcgatccagttttaaaagc
12	ctcctaattaattaattcccattttatactg
13	cctgatttaagcgatccag

676

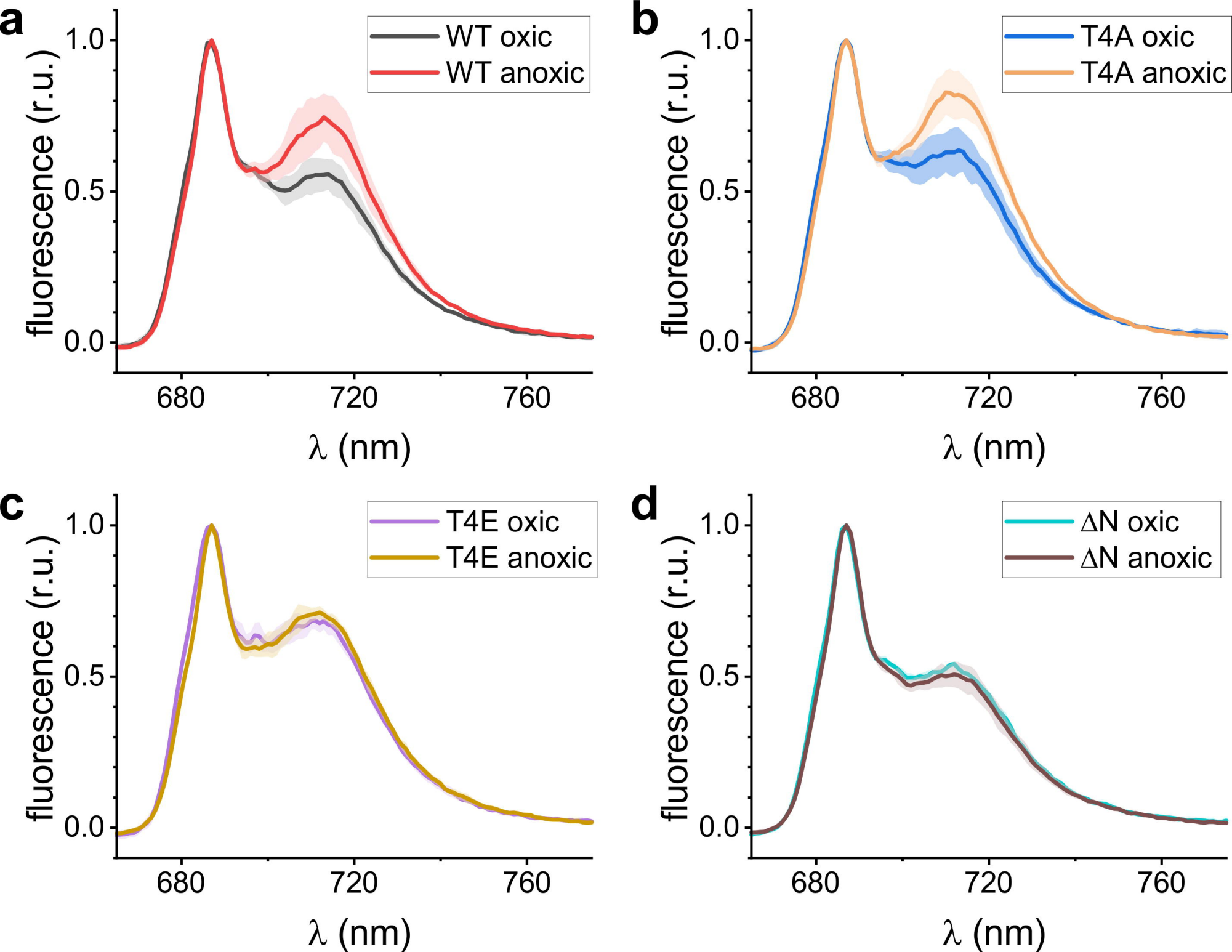
a
WT oxic
WT anoxic
fluorescence (r.u.)
1.0
0.5
0.0
680
720
760
λ (nm)
b
T4A oxic
T4A anoxic
fluorescence (r.u.)
1.0
0.5
0.0
680
720
760
λ (nm)
c
T4E oxic
T4E anoxic
fluorescence (r.u.)
1.0
0.5
0.0
680
720
760
λ (nm)
d
ΔN oxic
ΔN anoxic
fluorescence (r.u.)
1.0
0.5
0.0
680
720
760
λ (nm)

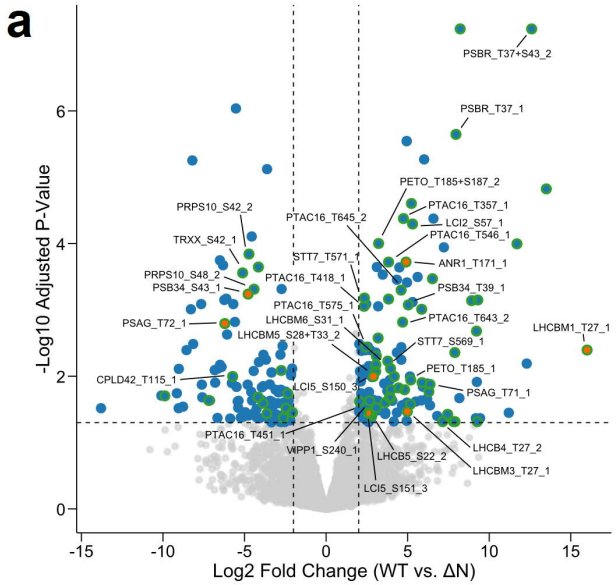
a
-Log10 Adjusted P-Value
Log2 Fold Change (WT vs. ΔN)
PSBR_T37+S43_2
PSBR_T37_1
PETO_T185+S187_2
PTAC16_T357_1
LCI2_S57_1
PTAC16_T546_1
ANR1_T171_1
PSB34_T39_1
PRPS10_S42_2
PTAC16_T645_2
TRXX_S42_1
STT7_T571_1
PRPS10_S48_2
PTAC16_T418_1
PSB34_S43_1
PTAC16_T575_1
PTAC16_T643_2
PSAG_T72_1
LHCBM6_S31_1
LHCBM1_T27_1
LHCBM5_S28+T33_2
STT7_S569_1
PETO_T185_1
CPLD42_T115_1
LCI5_S150_3
PSAG_T71_1
PTAC16_T451_1
VIPP1_S240_1
LHCB5_S22_2
LHCB4_T27_2
LHCBM3_T27_1
LCI5_S151_3

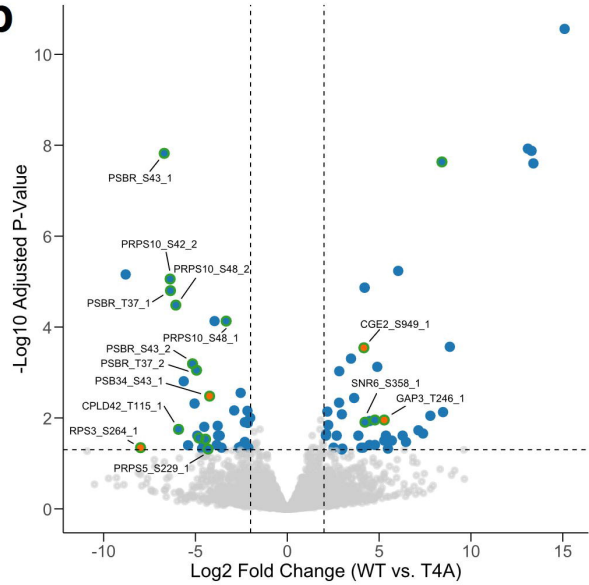
b
-Log10 Adjusted P-Value
Log2 Fold Change (WT vs. T4A)
PSBR_S43_1
PRPS10_S42_2
PRPS10_S48_2
PSBR_T37_1
CGE2_S949_1
PRPS10_S48_1
PSBR_S43_2
PSBR_T37_2
PSB34_S43_1
SNR6_S358_1
CPLD42_T115_1
GAP3_T246_1
RPS3_S264_1
PRPS5_S229_1

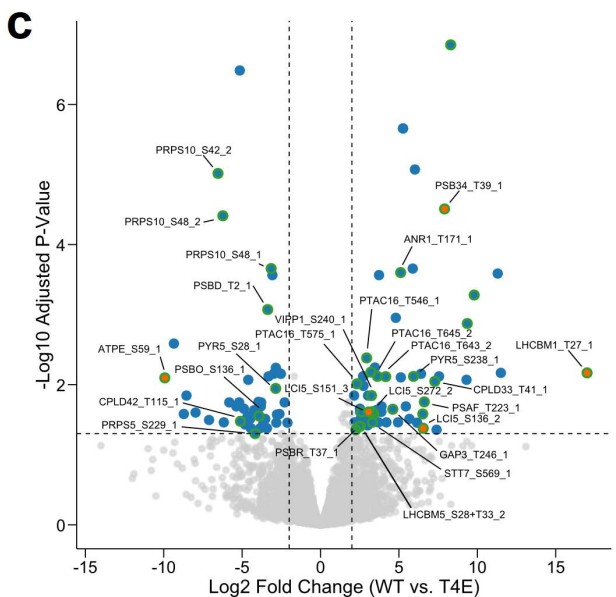
c
-Log10 Adjusted P-Value
Log2 Fold Change (WT vs. T4E)
PRPS10_S42_2
PSB34_T39_1
PRPS10_S48_2
ANR1_T171_1
PRPS10_S48_1
PSBD_T2_1
PTAC16_T546_1
VIPP1_S240_1
PTAC16_T575_1
PTAC16_T645_2
ATPE_S59_1
PYR5_S28_1
PTAC16_T643_2
LHCBM1_T27_1
PSBO_S136_1
PYR5_S238_1
LCI5_S151_3
LCI5_S272_2
CPLD33_T41_1
CPLD42_T115_1
PSAF_T223_1
PRPS5_S229_1
LCI5_S136_2
PSBR_T37_1
GAP3_T246_1
STT7_S569_1
LHCBM5_S28+T33_2

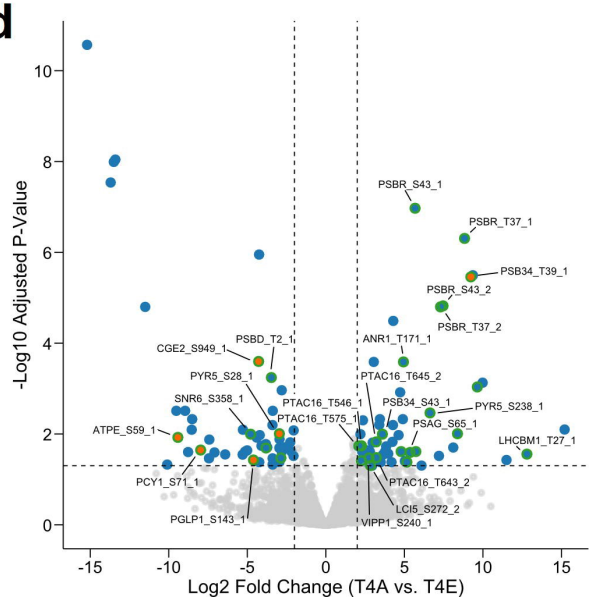
d
-Log10 Adjusted P-Value
Log2 Fold Change (T4A vs. T4E)
PSBR_S43_1
PSBR_T37_1
PSB34_T39_1
PSBR_S43_2
PSBR_T37_2
ANR1_T171_1
CGE2_S949_1
PSBD_T2_1
PTAC16_T645_2
PYR5_S28_1
SNR6_S358_1
PTAC16_T546_1
PSB34_S43_1
PYR5_S238_1
PTAC16_T575_1
PSAG_S65_1
ATPE_S59_1
LHCBM1_T27_1
PCY1_S71_1
PTAC16_T643_2
LCI5_S272_2
PGLP1_S143_1
VIPP1_S240_1

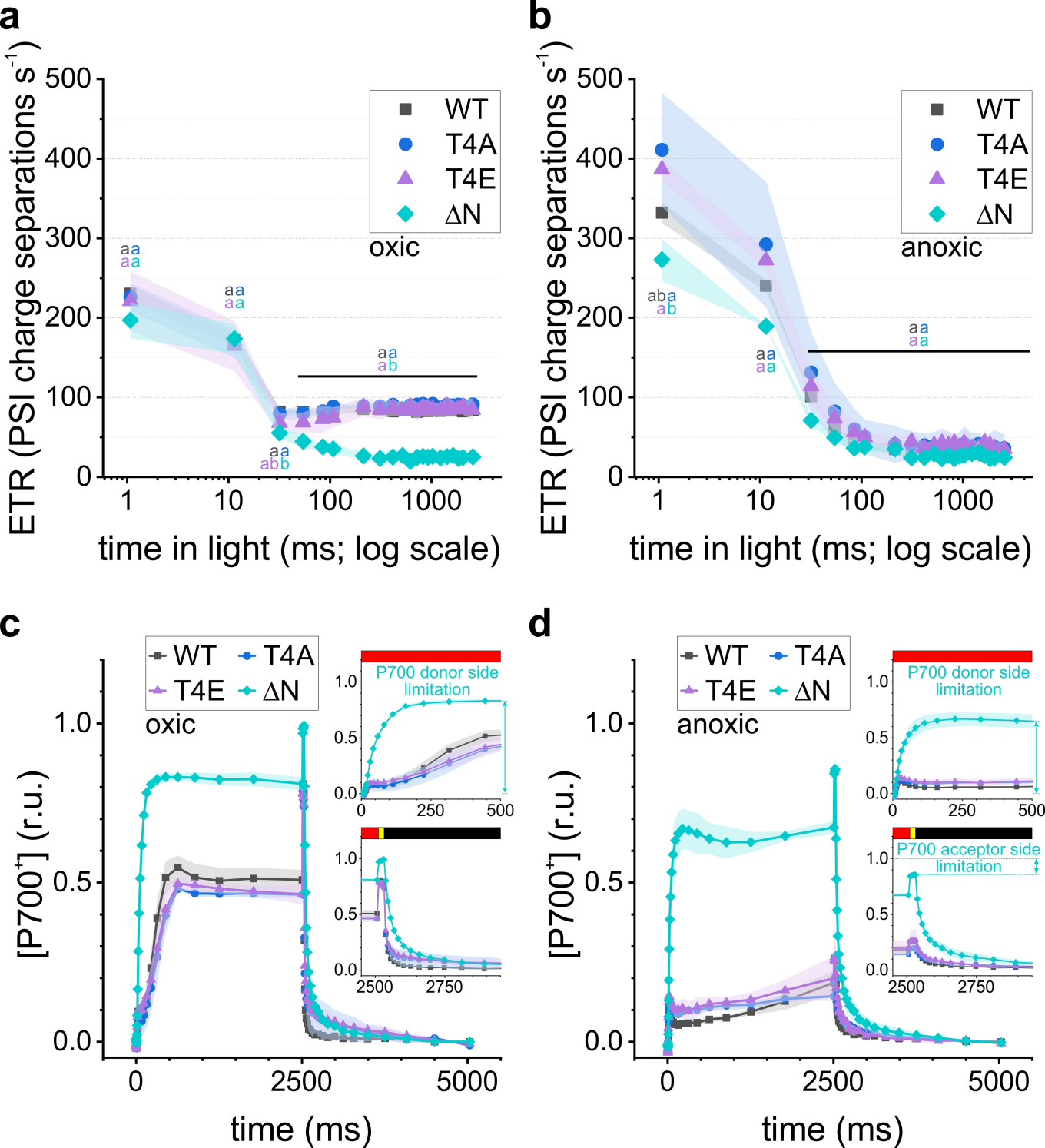
a
b
c
d
ETR (PSI charge separations s-1)
time in light (ms; log scale)
WT
T4A
T4E
ΔN
oxic
anoxic
[P700+] (r.u.)
time (ms)
P700 donor side limitation
P700 acceptor side limitation

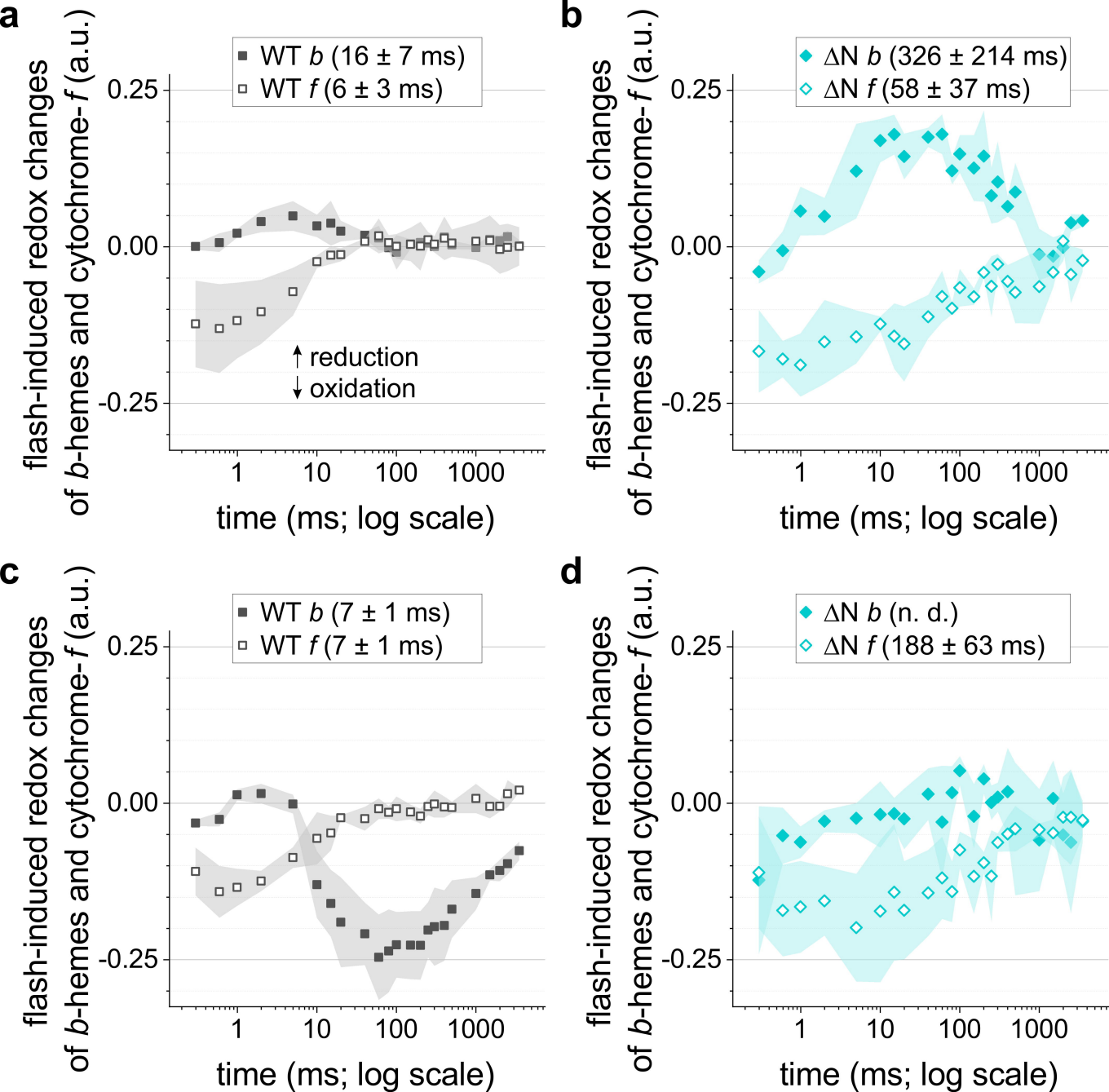
a
WT b (16 ± 7 ms)
WT f (6 ± 3 ms)
↑ reduction
↓ oxidation
b
ΔN b (326 ± 214 ms)
ΔN f (58 ± 37 ms)
c
WT b (7 ± 1 ms)
WT f (7 ± 1 ms)
d
ΔN b (n. d.)
ΔN f (188 ± 63 ms)
flash-induced redox changes of b-hemes and cytochrome-f (a.u.)
0.25
0.00
-0.25
1
10
100
1000
time (ms; log scale)